

Flight Testing Designs in HEXAFLY-INT for High-Speed Transportation

Johan Steelant, V. Villace, Alexander Kallenbach, A. Wagner, Jean-Yves Andro, S. Di Benedetto, B. Saracoglu, S.L. Chernyshev, A.A. Gubanov, V.A. Talyzin, et al.

▶ **To cite this version:**

Johan Steelant, V. Villace, Alexander Kallenbach, A. Wagner, Jean-Yves Andro, et al.. Flight Testing Designs in HEXAFLY-INT for High-Speed Transportation. HISST 2018, Nov 2018, MOSCOU, Russia. hal-01978022

HAL Id: hal-01978022
https://hal.science/hal-01978022

Submitted on 11 Jan 2019

HAL is a multi-disciplinary open access archive for the deposit and dissemination of scientific research documents, whether they are published or not. The documents may come from teaching and research institutions in France or abroad, or from public or private research centers.

L'archive ouverte pluridisciplinaire **HAL**, est destinée au dépôt et à la diffusion de documents scientifiques de niveau recherche, publiés ou non, émanant des établissements d'enseignement et de recherche français ou étrangers, des laboratoires publics ou privés.

HiSST: International Conference on High-Speed Vehicle Science & Technology
26–29 November 2018, Moscow, Russia

Flight Testing Designs in HEXAFLY-INT for High-Speed Transportation

J. Steelant[1], V. Villace[1], A. Kallenbach[2], A. Wagner[2], J.-Y. Andro[3], S. di Benedetto[4], B. Saracoglu[5], S.L. Chernyshev[6], A.A. Gubanov[5], V.A. Talyzin[5], N.V. Voevodenko[5], N.V. Kukshinov[7], A.N. Prokhorov[6], N. V. Grigoriev[8], A.J. Neely[9], D. Verstraete[10] and D. Buttsworth[11]

Abstract

Civil high-speed passenger transport only makes sense when deployed for long-haul intercontinental flights. Consequently, the related development and deployment of such a high-speed vehicle will most likely demand an international approach. The internationally funded HEXAFLY-INT project is a first step in the direction of civil high-speed transportation along with an international development where flight-testing is the focal point.

The global aim is to flight test an experimental waverider-based vehicle concept above Mach 7 to verify its potential for a high cruise efficiency during a free-flight. In parallel, the concept will also be flight tested to prove the waverider concept is also able to take-off, to accelerate to subsonic speed and to land in an efficient and robust way.

The feasibility for a 3m long vehicle was demonstrated during the European precursor project HEXAFLY. Its realization is now being enabled on an international scale preparing the grounds for global cooperation in case of a future deployment of a high-speed cruiser. These flight opportunities will increase drastically the Technology Readiness Level of developments realized in previous high-speed EC projects such as ATLLAS I & II and LAPCAT I & II. The present paper describes the various numerical and experimental investigations carried out so far by the different international partners.

Keywords: *high-speed, multi-disciplinarity, vehicle design, waverider, flight-testing, hydrogen*

Nomenclature

ATLLAS – Aero-Thermal Loaded Material Investigations for High-Speed Vehicles
BL - Boundary Layer
BLT - Boundary Layer Transition
CFD - Computational Fluid Dynamics
EC – European Commission

[1] *ESA-ESTEC, Flight Vehicle and Aerothermodynamics Engineering Section TEC-MPA, P.O. Box 299, Noordwijk, Netherlands, Johan.Steelant@esa.int, Victor.Fernandez.Villace@esa.int*
[2] *Deutsches Zentrum für Luft- und Raumfahrt (DLR), Mobile Rocket Base Munich and Institute of Aerodynamics and Flow Technology, Göttingen, Germany, Alexander.Kallenbach@dlr.de, Alexander.Wagner@dlr.de*
[3] *ONERA (French Aerospace Research Centre), Design & Assessment of Aerospace Vehicles Unit, Chemin de la Hunière – BP 80100, FR-91123 Palaiseau Cedex, France, jean-yves.andro@onera.fr*
[4] *Centro Italiano Ricerche Aerospaziali (CIRA), Via Maiorise 81043, Capua (CE), Italy, s.dibenedetto@cira.it*
[5] *Von Karman Institute, Waterloose Steenweg 72, St. Gen. Rode, Belgium, saracog@vki.ac.be*
[6] *Central Aerohydrodynamic Institute (TsAGI), Research and Production Complex, Zhukovsky, Moscow region, 140180 Russia, anatoly.gubanov@tsagi.ru, nina.voevodenko@tsagi.ru, talyzin@tsagi.ru,*
[7] *Central Institute for Aviation Motor (CIAM), 2 Aviamotornaya street, Moscow, 111116 Russia, kukshinov@ciam.ru, prokhorov@ciam.ru*
[8] *Gromov Flight Research Institute (LII), Zhukovsky, Moscow region, 140180 Russia, nio7@lii.ru*
[9] *Univ. of New South Wales (UNSW), School of Engineering and Information Technology, Canberra, A.Neely@adfa.edu.au*
[10] *Univ. of Sydney, School of Aerospace, Mechanical and Mechatronic Engineering, Building J07, Maze Crescent, Darlington Campus, NSW 2006, Australia, tamas.bykerk@sydney.edu.au, dries.verstraete@sydney.edu.au*
[11] *Univ. of Southern Queensland, School of Mechanical and Electrical Engineering, david.buttsworth@usq.edu.au*

Copyright © 2018 by the author(s)

EFTV – Experimental Flight Test Vehicle
ESM – Experiment Support Module
HEXAFLY – High-Speed Experimental Fly Vehicles
HXI – HEXAFLY-International
LAPCAT – Long-Term Advanced Propulsion Concepts and Technologies

Greek
α – Angle of Attack
Superscripts
* – total values
Subscripts
ref – reference
0 – total values

1. Introduction

The overall objective of HEXAFLY is to create a generic high-speed platform enabling in-flight testing of several breakthrough technologies. To mature this idea, a scientific mission profile was worked out based upon a preliminary design of a high-speed flight test vehicle along with the identification of the most promising flight platform, e.g. sounding rocket. This combination would then offer the possibility to test out various technologies, grouped around the six major axes of HEXAFLY:

1. *High-Speed Vehicle Concepts* to assess the overall vehicle performance in terms of cruise-efficiency, range potential, aero-propulsive balance, aero-thermal-structural integration, etc...
2. *High-Speed Aerodynamics* to assess aerodynamic vehicle shapes with high L/D, aerodynamic manoeuvrability, stability, etc…
3. *High-Speed Propulsion* to evaluate the performances of high-speed propulsive devices such as intakes, air-breathing engines, nozzles including phenomena such as high-speed combustion, injection mixing processes, etc…
4. *High-Temperature Materials and Structures* to flight-test under realistic conditions high temperature lightweight materials, cooling concepts, reusability aspects…
5. *High-Speed Flight Control* requiring real-time testing of Guidance Navigation Control in combination with technologies on Health Monitoring Systems/ Fault Detection and Isolation
6. *High-Speed Environmental Impact* focusing on reduction techniques for sonic boom and sensitivities of high-altitude emissions of H_20, CO_2, NOx on the stratosphere.

Following this general HEXAFLY philosophy, a first project on international level was proposed, *HEXAFLY-INTernational,* with the auspices of the European Community (EC) together with 11 partners from Europe (ESA, AIRBUS, CIRA, DLR, ONERA, TET, TSD, GDL, Marotta, Univ. of Stuttgart, VKI), 4 from the Russian Federation (TsAGI, CIAM, LII and MIPT) and 3 from Australia (Univ. Sydney, UNSW, USQ). The overall aim is to design, manufacture and flight test a high-speed vehicle, based on the configuration developed in previous EC co-funded projects ATLLAS I & II [1][2][3], LAPCAT I & II [4][5], and HEXAFLY [6][7]. Under HEXAFLY-INT, both a glider and a hydrogen-propelled variant of the high-speed vehicle are being considered, the former being developed by EC partners with international partners, the latter being developed only by the Russian partners. The flight experiment carried out by the Europeans, Russians and Australians, is focused on

- Elaborating a self-controlled glider demonstrating a high aerodynamic efficiency in combination with a high internal volume
- a positive aerodynamic balance at a cruise Mach number of 7 to 8 in a controlled way
- making optimal use of advanced high-temperature materials and/or structures
- the aerodynamic gliding performance from Mach 8 down to Mach 2
- including several breakthrough technologies on-board [10],
- validating methods and technologies deployed in hypersonic vehicles design [7][10][11][12][14].

Two distinctly different flight tests are considered. One at high-speed checking the cruise capability of a potential civil passenger hydrogen fuelled high-speed vehicle, another at low-speed to check its handling qualities during take-off and landing.
The Experimental Flight Test Vehicle (EFTV), for testing the cruise performance as a non-propelled glider at high-speed will be launched by a sounding rocket (the Brazilian VS43 launcher based upon an 8-ton solid rocket motor) in a suborbital trajectory having an apogee at about 90 km (Fig. **1**). After the release from the launcher, the EFTV will perform the first part of the descent docked to the Experimental Service Module (ESM), which controls the vehicle attitude. As soon as the EFTV features full aerodynamic control authority, it undocks from the ESM and pulls out from its descent to perform a

Copyright © 2018 by the author(s)

hypersonic cruise at approximately Mach 7. In this experimental phase, the EFTV aims to demonstrate as a glider a high aerodynamic efficiency (L/D≥4), a positive aerodynamic balance at controlled cruise Mach numbers (7÷8) and an optimal use of advanced high-temperature materials and structures. The overall mission requirements are listed in Table 1.
The vehicle design, manufacturing, assembly and verification are the main drivers and challenges in this project in combination with a sounding rocket tuned for the mission. Both the glider and the propelled options of the HEXAFLY-INT high-speed vehicle are characterized from the aerodynamic and aerothermodynamic points of view.

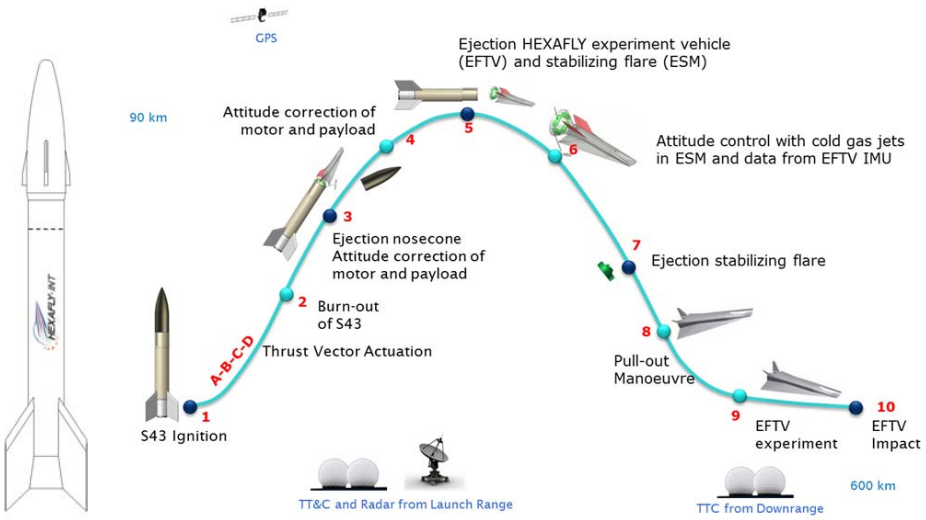


Fig. 1 HEXAFLY-INT VBS-43 launch vehicle (left) and overall mission profile (right).

Table 1: Basic mission requirements for EFTV

Requirement	Target Value	Min. Value	Max. Value	Comment
Phase I: insertion into level flight: Mach number [-]	7.4	7	8	Phase I: addressing aerodynamic balance after pull-out manoeuvre
Phase II: Gliding Phase: ➔ **Flight Mach number [-]**	5 to 7.4	2	8	Phase II: Mach number gradually dropping during gliding phase potentially including manoeuvres.
Flight altitude [km]	30	27	33	Optimal: level flight
Flight path angle [°] Phase I	0 (level)	0	10 to 15 (TBD)	Accuracy: 0.1 (measured) Accuracy: +/-5 (TBD) for insertion
Test time (Phase II) [s]	Max. possible	150	Till impact	Gliding Phase duration defined by aero-stability range

Besides the high-speed flight experiment, an additional low-speed flight experiment will be performed to crosscheck the viability of the vehicle concept for later deployment as passengers' aircraft. It entails a flight experiment in the Danger Area 451 (Univ. of Sydney) to verify the take-off, cruising at a low subsonic speed and landing potential for the waverider-based vehicle and its related control authority.

The program was kicked off in April 2014 and will pass the CDR by end of 2018. The paper describes the status of the vehicle design along with the elements related to the flight preparation.

In parallel to the overall technical work to realize the different flights and experiments, a framework has been set up to ease the exchange of students of the involved universities among the different partners. This gives them a unique expertise of contributing to the different pieces of one of these flight experiments.

Copyright © 2018 by the author(s)

2. Glider Concept

2.1. General Layout of the Experimental Flight Test Vehicle (EFTV)

The EFTV, see Fig. **2**, is a hypersonic glider of 3.29m length and having a span of about 1.23m. The EFTV has a two-dimensional nosetip with 2mm rounding and 2mm lateral fillet, while the wing is characterized by a 80° sweep angle and 14° negative dihedral angle, and 1mm rounded leading edge. As control surfaces, the vehicle is equipped by a couple of active ailerons (0.4m long and 0.32m wide), which can be deflected in symmetric and asymmetric way, and a couple of fixed vertical fins characterized by a 68.5° sweep angle and a 54° angle formed between the two fins in the transversal plane. The present aeroshape is the result of an evolution [10] that, following the suggestions by the continuous aero-heating assessment, has affected mainly the nosecap and forebody configuration, the wing (leading edge and fuselage intersection) and the aileron.

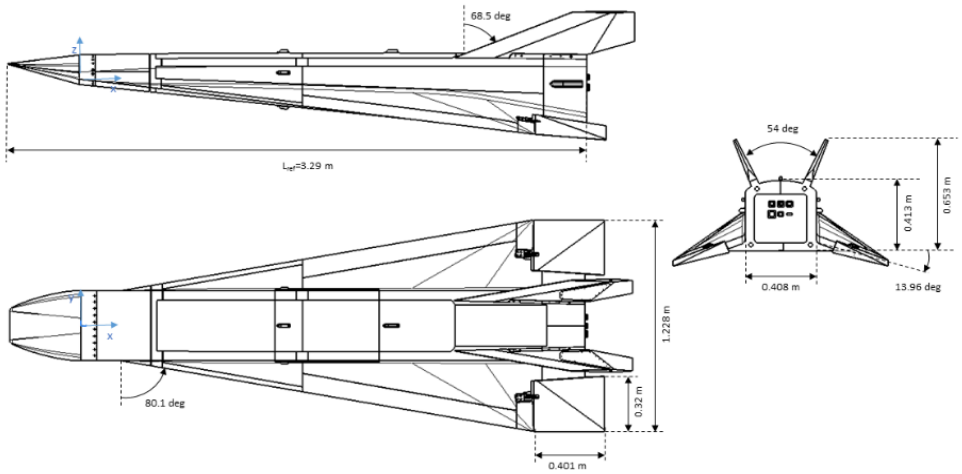


Fig. 2: EFTV three-view drawing

During ascent and first part of the re-entry phase after release from the rocket at the 90km apogee, the EFTV is coupled with the conically shaped Experiment Service Module ESM, which has a double function (Fig. **3**). At first, it acts as the interface between the EFTV and the Launch Vehicle Service Module (LVSM) mounted on top of the S43 booster. Secondly, it will act as a weathercock aligning the EFTV to a certain attitude at 55km altitude from which it will then separate. It allows the EFTV to start its pull-out manoeuvre to bring the EFTV to a hypersonic levelled flight above Mach 7 and execute its overall mission objectives starting from a 30km altitude. A typical trajectory is given in Fig. **4**. The ESM has also a Cold Gas System (CGS) on-board to assure attitude control in the exo-atmosphere once released from the LVSM.

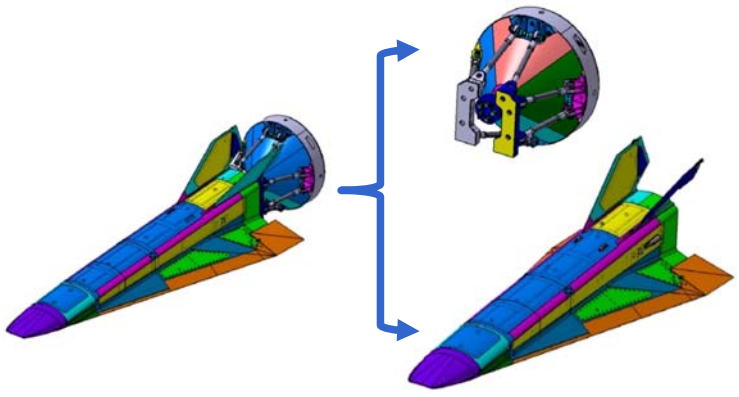


Fig. 3: The EFTV glider with ESM.

Copyright © 2018 by the author(s)

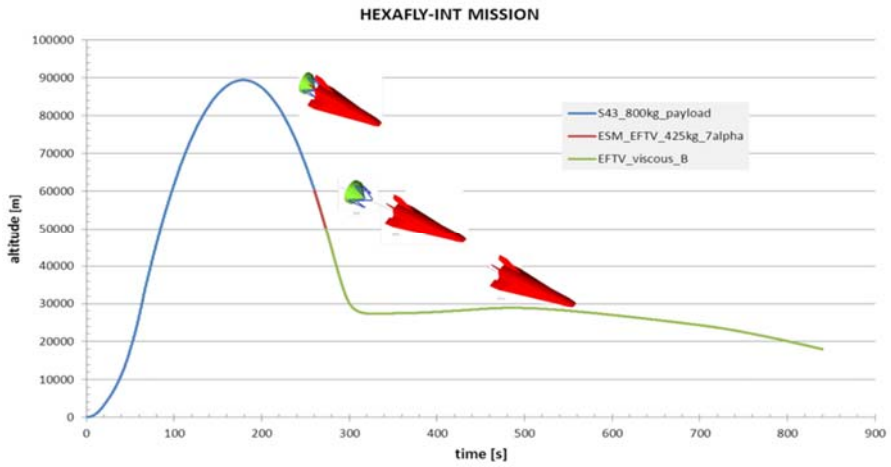


Fig. 4: Altitude time history

As general material layout, the metallic structure of the EFTV, i.e. the fuselage, wing and vertical tail, is composed of titanium alloy, apart from the copper nose section. Wing leading edges and ailerons are in C/C-SiC (Fig. 5). The metallic exposed surface parts are thermally protected by high emissivity or ZrO_2 coatings. This material layout is compliant with the aerothermal loading conditions expected for the glider.

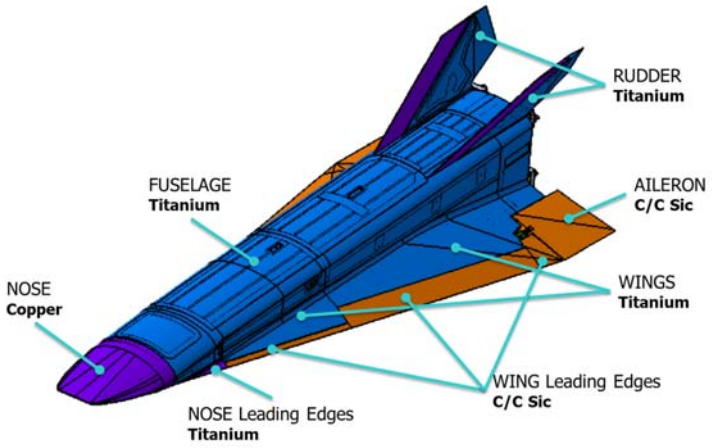


Fig. 5: Material composition of EFTV

The EFTV will be equipped with an avionic system composed of an inertial measurement unit, a GPS, two servo-actuators for the ailerons, and a flight control computer, which will ensure the on-board mission management. The vehicle will also be equipped with an in–flight measurement system acquiring pressure, temperature and acceleration data sensors for the sake of post flight analysis and simulation tools validation. The on-board avionics will also include a downlink telemetry system (i.e. with antennas) which will transmit all mission data to the Ground Control Station at the launch site. The overall layout of the EFTV vehicle is shown in Fig. 6.

In Fig. 7, the exploded view of the fuselage sections and the major components are shown. The fuselage structure is mainly composed by milled frames, upper beams and panels. The assembly of the fuselage structure is realized by joining the upper beam frames and lower panels with fixed bolts. The upper panels are joined to the frames and upper beams by removable bolts in order to allow easy access to the equipment located inside the fuselage. The tail fuselage is composed by two shells and a rear panel. The upper part is joined with a bolted strap whereas the bottom part is joined with an overlap between the two shells by two fixed bolts. The rear panel is bolted with removable bolts allowing access to the internal part of fuselage. The tail fuselage shells also include the provision for the pyro bolts installation. Further details on the multi-disciplinary design issues and related analyses can be found in [21].

Copyright © 2018 by the author(s)

ITEM N°	DESCRIPTION	QTY
1	EBX1	1
2	AHRS MAGNETOMETRO	1
3	BATTERY_BOX_(4_strings)	2
4	EBX	1
5	S-BAND-TV-SENDER-S2460	2
6	S-BAND-SENDER_S 2412	2
7	S-BAND-ANTENNA HT	2
8	TC-KOPPLER	1
9	S-BAND COUPLER	1
10	IMU	1
11	FCC	1
12	GPS-BOX	1

ITEM N°	DESCRIPTION	QTY
13	TSD_PMS	1
14	ACTUATOR	2
15	TC ANT-Antenna Cover	2
16	TC ANT-450-TECOM	2
17	TC-Empfänger-UHF E450	2
18	GPS-ANTENNA_SHEFEX	1
19	HF DAQ BOX 4 STACKS	1
20	HF DAQ BOX 4 STACKS	1
21	UNSW BOX	1
22	ACTUATOR E BOX	2
23	MONOCHROME CAMERA	1

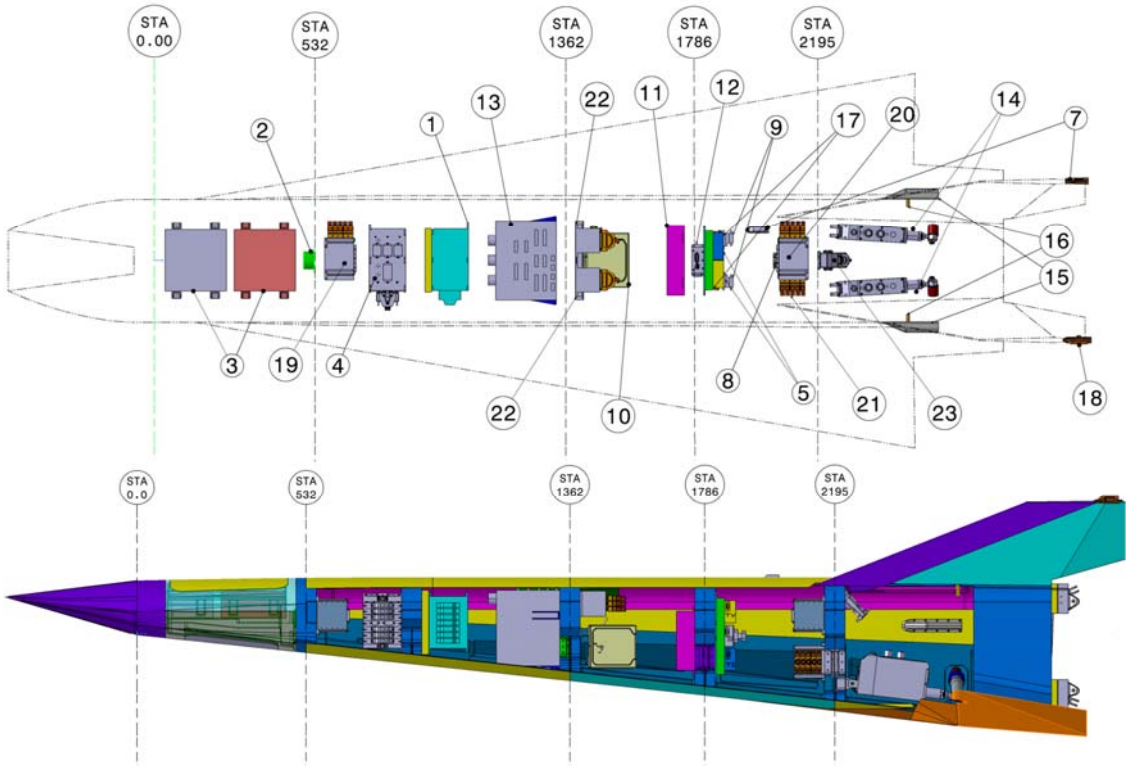


Fig. 6: Overall EFTV Layout

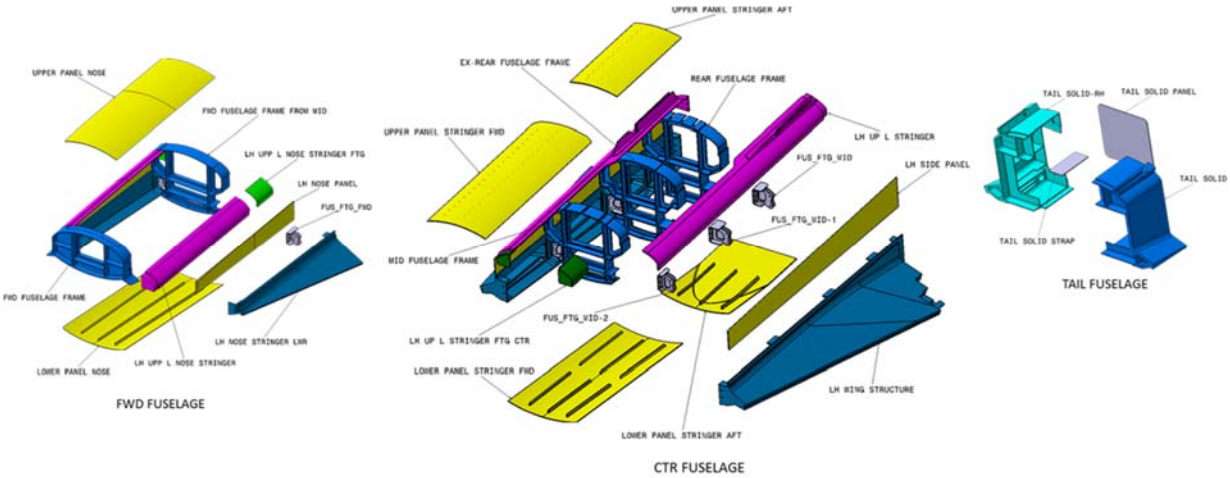


Fig. 7: Exploded view of EFTV

Copyright © 2018 by the author(s)

2.2. Flight Control

Being launched from Alcântara in Brazil, Fig. 8 shows a typical trajectory of the launcher (yellow) and the EFTV (green). Due to launch range constraints and telemetry limitations, the EFTV needs to remain within 600km from the coastline to assure the on-board collection of the experimental data is entirely transmitted to a ground station. Apart from a pull-ut manoeuvre and a gliding phase, a banking manoeuvre is carried out assuring the vehicle remains within the range of the ground station (see [20] for further details). To carry out these different manoeuvres, an actuation system needs to be designed to cope with these different loads.

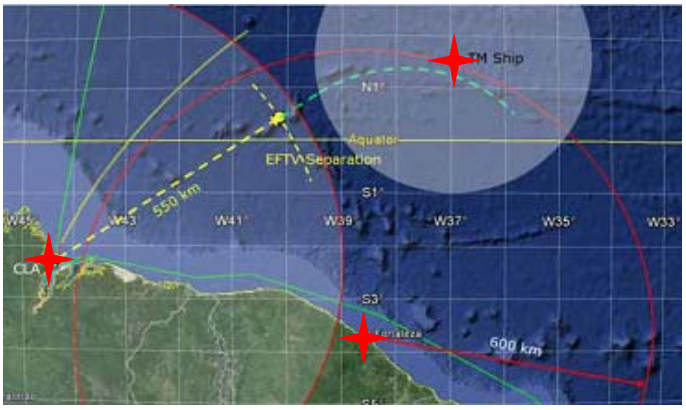


Fig. 8: Typical trajectory: launch ascent (yellow), EFTV gliding phase (green)

One the most critical specifications is the maximum hinge moment that the actuation system should be able to withstand during the pull-out manoeuver. A value of nearly 300 Nm was used for sizing the complete actuation system (see Fig. 9). The elevon and the main portion of the torsion bar are designed as a single CMC block. The CMC bar passes through the fuselage bearing and ends with a titanium insert providing an interface with the titanium lever arm.

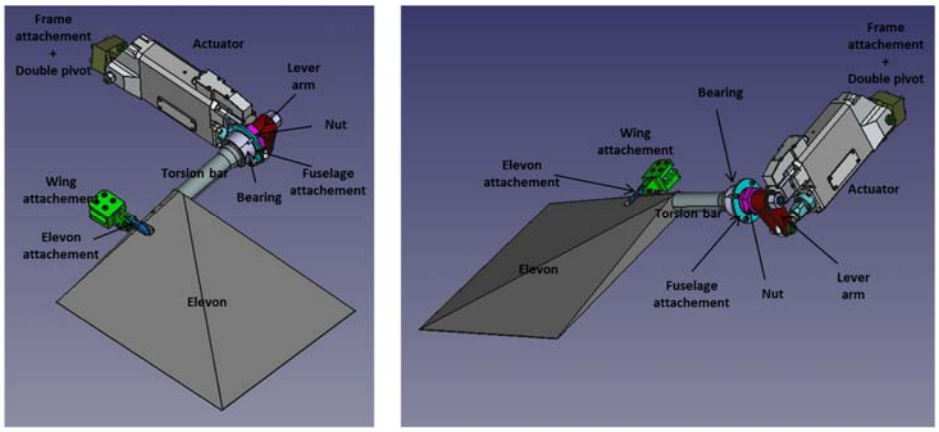


Fig. 9: Actuation System general design

Experimental tests indicated that the CMC torsion bar would be able to withstand above 400 Nm before failure (Fig. 10). The French ISP society was selected to provide off-the-shelf servo-actuators, customized to withstand all mechanical loads and vacuum conditions. Details are provided in [23].
To guarantee the lateral stability, two large vertical tails are mounted on the rear. As they are constructed entirely from Titanium, it is necessary to minimize their weight by topology optimization, i.e. finding find the best location to place structure in a pre-defined design domain that is subjected to known loading and boundary conditions. The final structure (Fig. 11) was determined by optimising for all 12 load cases and implementing non-designable regions towards the trailing edge where the thickness of the fin goes below a certain value such that manufacturing cut-outs in this region is not feasible and near the dovetail where cut-outs are not permitted. The final mass of the vertical fin is 12.8kg, this is a 45% weight reduction, resulting in a total weight saving of 20.88kg. The maximum

Copyright © 2018 by the author(s)

stress found in the proposed vertical fin design is 412MPa occurring at t=47s after the release of the EFTV from the ESM. Further details can be found in [24].

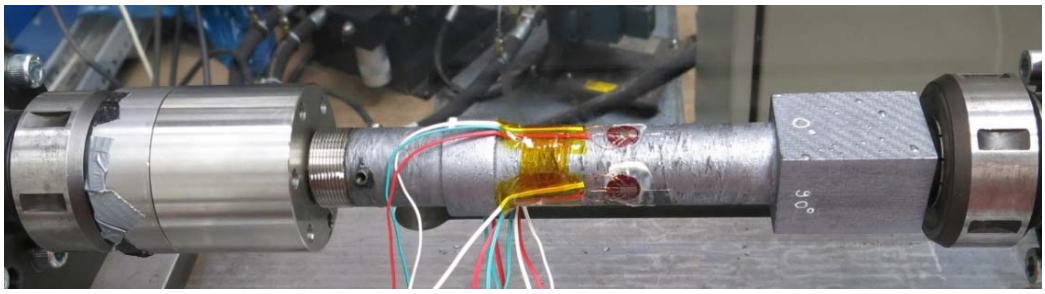


Fig. 10: CMC torsion bar and CMC block on torsion test rig

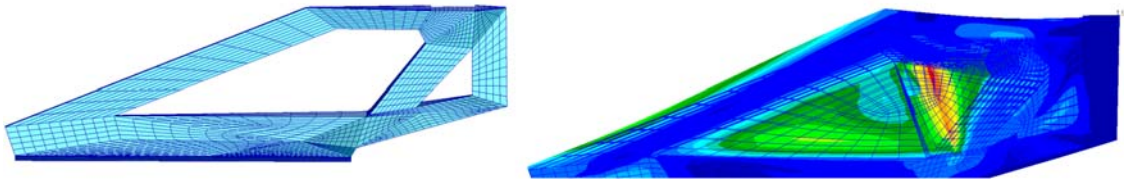


Fig. 11: Proposed final internal structure for vertical fin (left) and stress distribution at max. stress

2.3. In Flight Measurement

The EFTV vehicle is equipped with various sensors, which are processed on-board and instantaneously transmitted to the ground. The sensor positions are shown in Fig. 12 and entail heat flux (HF), thermocouples (TC), Pressure ports (PP), Strain gauges (SG), Coaxial Thermocouple (CT) and accelerometers (AC). A particular set is related to the Flush Air Data System (FADS), which consists of 10 pressure ports in the nose. They will serve as post processing the attitude of the vehicle. The overall cabling is simplified by using breakout boxes, which connect, collect and distribute the data and power from the DAQ boxes to the sensors.

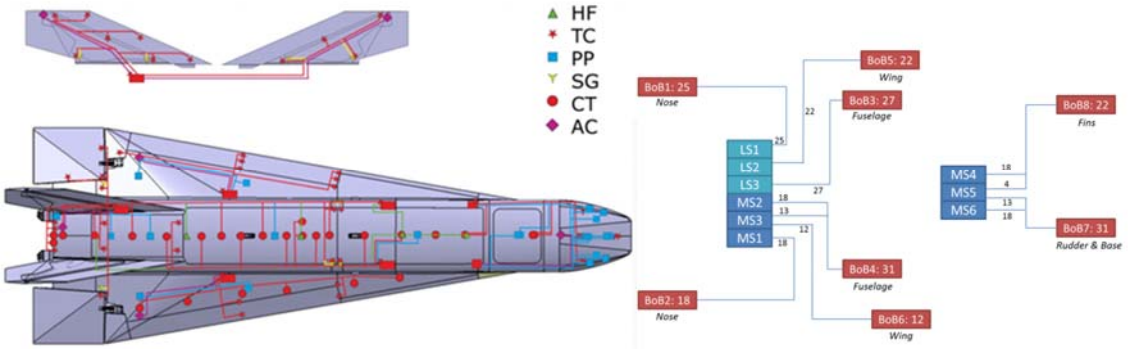


Fig. 12: Cabling and positioning schema of the sensors (left) and DAQ-system distribution (right)

2.4. Thermal Management

As a low cost demonstrator, the main structure of Hexafly-Int vehicle is mostly metallic. The chosen material is a Russian variant of titanium alloy, named BT-20, which is able to withstand 700°C and even higher values for shorter periods along the reference trajectory. The assessed solutions for the external Thermal Protection System (TPS) were: (i) heat sink by increasing the titanium thickness (ii) Prosial ® coating (iii) zirconium coating (iv) high emissivity black paint (ε>0.8).

Copyright © 2018 by the author(s)

A high emissivity paint (ε>0.8) was found as a sufficient solution for maintaining the temperature of the fuselage panels below 700°C. This paint even allows further reducing the thickness of the leeside panels. At stagnation regions such as the copper nose, root wing and the Ti-leading edges of the vertical tail, additional protection by ZrO2 is needed.
Heating of the internal titanium structure along the trajectory was assessed in [8][9][15]. Fig. 13 shows the maximum temperature distribution obtained for the frames. They were considered not too hot allowing internal equipment to be fixed directly onto them.

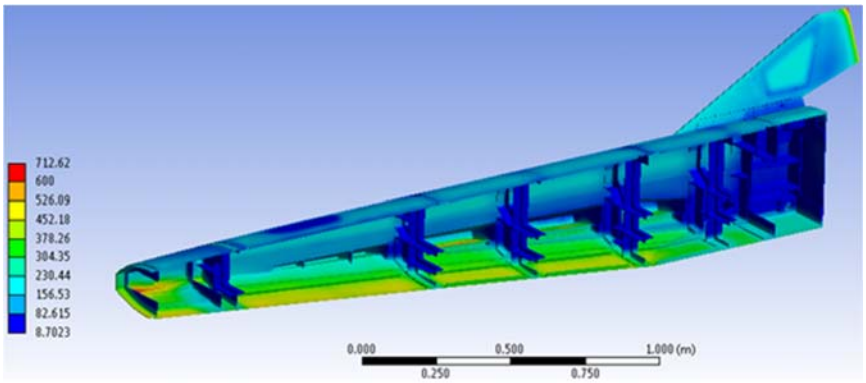


Fig. 13: Maximal temperature distribution on the titanium internal structure

The main source of equipment heating is the thermal radiation coming from the panels of the structure. ONERA and ESA designed an internal thermal protection system based on a light flexible microporous insulator named Aeroguard® provided by PROMAT firm in Belgium. This material is able to withstand 1000°C and it exhibits an extra low thermal conductivity at sea level and is even further reduced at high altitude (lower pressure). The thermal control system is composed of two layers of 9 mm thick Aeroguard 160 ® panels, which are kept in place with respect to the structure thanks to only thin wires fixed at their extremities to the internal frames of the structure (Fig. 14). This smart fixation allows fast depressurization of the insulation panels and optimization of the mass while withstanding mechanical vibrations during the boosted phase of the flight. The detailed discussion on thermal management is worked out in [22].

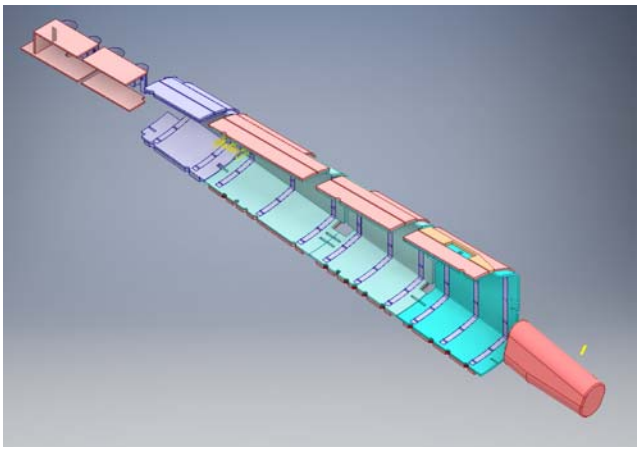


Fig. 14: Customized internal thermal protection system along the different bays

2.5. Aerodynamic Performance

2.5.1. Numerical Aerodynamic Evaluation

The numerical aerodynamic database generation is carried out by CIRA, DLR, ESA and TsAGI. In the early design phase, only inviscid CFD computations were performed and a preliminary AErodynamic DataBase (AEDB) of the EFTV configuration was setup by DLR-Braunschweig [11] with the goal to provide aerodynamic performance for the first Flight Mechanics analyses and to check the vehicle longitudinal and lateral-directional static stability. In fact, it had to be verified that vehicle aerodynamic

Copyright © 2018 by the author(s)

surfaces were able to provide sufficient lift at hypersonic atmospheric entry to stay within the load constraints during descent and reach the envisaged altitude corridor to realize the first phase objectives. Aerodynamic coefficients were provided as a function of Mach number, angle of attack, sideslip angle, and aileron deflections.

The Mach range from 2 to 9 was analysed for the EFTV only in the continuum regime with air modelled as an ideal gas. An example of inviscid aerodynamic assessment is shown in Fig. 15. As summarized in Ref. [11], the EFTV aeroshape features rather high lift-to-drag ratios at hypersonic speeds. No significant effects of sideslip on aerodynamic efficiency and total pitching moment for both clean and deflected aileron configurations were predicted. Numerical results clearly underline that the glider is statically stable in longitudinal flight at all Mach numbers under investigation and for all the angles of attack, sideslip, and aileron deflections considered so far.

Further, results also pointed out that the aeroshape seemed to be trimmable in all the flight conditions investigated [11], also for supersonic Mach numbers and higher angles of attack. Finally, static stability in lateral-directional flight conditions is also confirmed since at all Mach numbers it is verified that $C_{Y\beta}<0$, $C_{n\beta}>0$ and $C_{l\beta}<0$ (the last one only for positive angles of attack) [11]. As a conclusive result, the preliminary AEDB pointed out the compliance of the hypersonic glider's aerodynamic performance with the expected flight envelope.

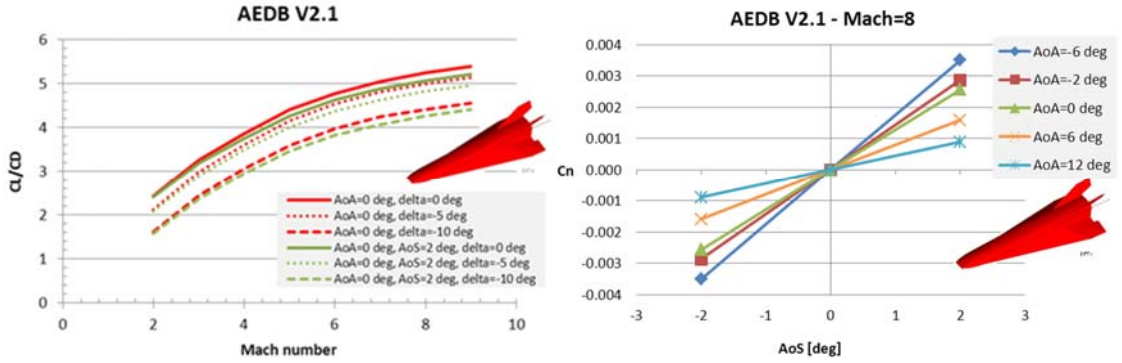


Fig. 15: The L/D vs. Mach (left) and yaw moment coefficient versus sideslip (right) at different attitudes.

The preliminary mission trajectory was generated by DLR-Moraba for the ascent phase assuming a total payload mass of 800kg (EFTV, ESM, launch vehicle service module, fairing). The descent trajectory was assessed by GDL considering a "train" EFTV+ESM from apogee down to 55km altitude and then followed by only the EFTV after its separation from the ESM. A number of 3 degree-of-freedom (DoF) planar trajectories were generated for the hypersonic glider. EFTV's AoA initial schedule was based on a profile that satisfies control authority criteria. Trajectory labelled B-viscous (see Fig. 16) was finally selected as reference, being the lower reference trajectory of the flight corridor having a built-in margin during future trajectory consolidation, and preliminary EFTV/ESM separation was fixed at 55km altitude to satisfy typical control authority criteria.

CIRA, ESA and TsAGI have finalized Navier-Stokes (NS) CFD simulations to generate the final viscous AEDB. The complete CFD test matrix foresees more than 250 3-D Navier-Stokes simulations were carried out in laminar and fully turbulent flow conditions (Spalart-Allmaras one-equation eddy viscosity is being selected for turbulence modelling). Those CFD simulations are conceived to address the effects of Mach number, angle of attack, angle of sideslip, symmetric and asymmetric aileron deflection, Reynolds number, grid resolution, turbulence models, laminar-to-turbulent transition, code-to-code, and finally to verify trim conditions and aero-thermal loads along the reference trajectory. The AEDB includes also the model of uncertainties for aerodynamics and the dynamic derivatives data-package, thus providing inputs for flight mechanics, thermo-structural analysis (the aero-thermal loading conditions the EFTV has to withstand during the flight must be accurately verified) and in-flight experimentation layout optimization.

Copyright © 2018 by the author(s)

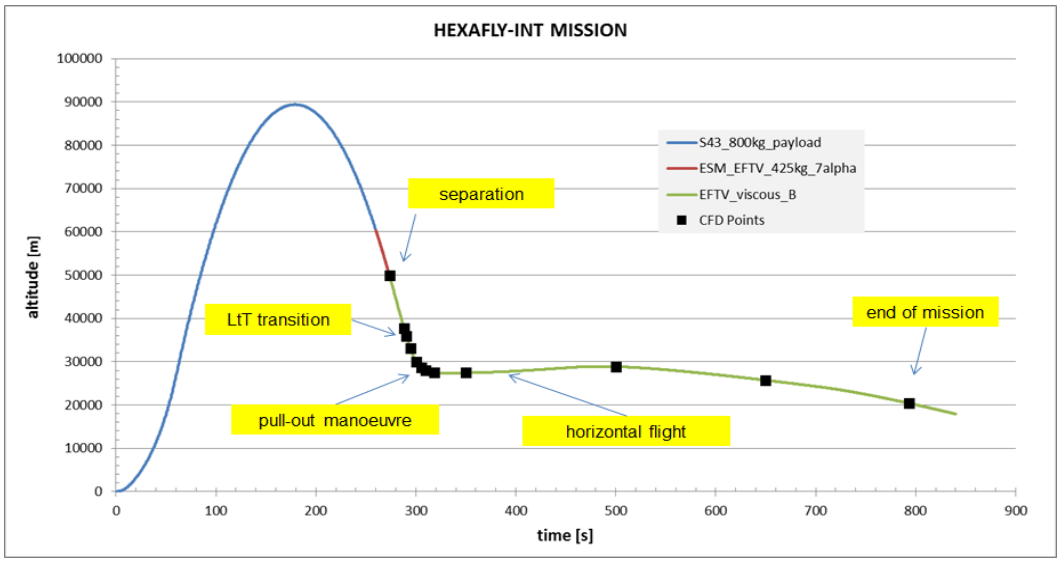


Fig. 16: Reference trajectory: altitude time history.

An exemplary hybrid computational grid (i.e. tetrahedrons in the flow and prisms inside the boundary layer) built for NS simulations is shown in Fig. 17. At least 10 million cells were necessary for a half configuration, and in the case of turbulent boundary layer assumption, the condition of Y^+=O(1) at wall was imposed. Surface temperature contours on the full vehicle during the descent and the effect of sideslip at high angle of attack, at Mach=7.5 are shown in Fig. 17. The hot nosetip, wing leading edges and fin leading edges as result of nearly attached shock waves are noticeable. From laminar boundary layer parameters extracted from CFD results to apply local natural and step-induced transition criteria along the reference trajectory [13], a fully turbulent flow was proposed at the altitude of about 30 km. More details on the aerodynamic database and related uncertainties can be found in [12][26].

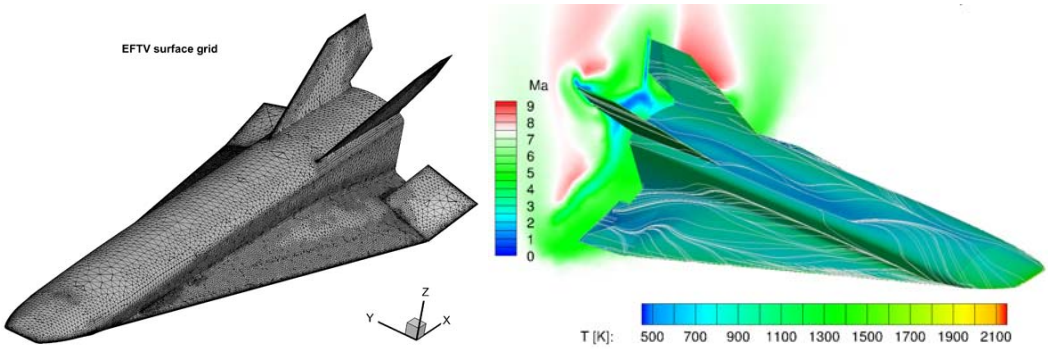


Fig. 17: Hybrid NS mesh (left) and EFTV surface temperature contours and skin-friction lines (Mach=7.5, AoA=10°, AoS=4°, clean configuration).

2.5.2. Experimental Aerodynamic Evaluation

The experimental test campaign on the aerodynamics of the EFTV glider configuration was performed at TsAGI in the supersonic and hypersonic wind tunnel T-116, characterized by a test chamber with a squared cross section of 1 m × 1 m size. The tests were performed with the model produced by TsAGI, whose scale was 0.35 w.r.t. the size of the EFTV. The model (Fig. 18) has allowed investigating aerodynamic characteristics of the vehicle with different settings of aileron's deflection.

The windtunnel campaigns in the T-116 at TsAGI have been performed in a Mach number range from 3 to 8 at angles of attack from – 6º to 12º. The freestream conditions are reported in Table 1 in terms of Mach number, total pressure P_{tot}, total temperature T_{tot} and unit Reynolds number Re_{1m}. The latter is adapted to the flight altitude H of the real EFTV vehicle and the model scale. The test conditions in T-116 are reasonably close to those expected along the flight trajectory of the EFTV vehicle (Fig. 16).

Copyright © 2018 by the author(s)



Fig. 18. The model of the EFTV Glider Option mounted on a sting.

Table 1. Flow conditions used in the Wind Tunnel T-116

Mach	**3.03**	**4.05**	**5.05**	**6.00**	**6.99**	**7.88**
P_{tot} [atm]	1.1	1.4	5	7.4	22	31.5
T_{tot} [K]	300	300	455	485	675	825
$Re_{1M}*10^{-6}$	7.74	5.96	6.88	6.32	7.66	5.92
Simulated Flight Altitudes:						
H [km]	24.8	28	28.4	30.5	30	32.5

An electromechanical balance measured the aerodynamic forces and moments. To correct for the sting in the rear, the base drag was excluded from the experimental data by measuring the base pressure on the model. Corresponding corrections were made by equalizing the base pressure to the free-stream static pressure. Corrections were also made for taking into account the effects of gravity and sting deformation during tests.

The main aerodynamic characteristics of the glider model without flap deflection and zero sideslip angle, i.e. aerodynamic drag force coefficient C_D,, aerodynamic efficiency L/D and pitching moment coefficient C_m are presented in Fig. 19 as function of angle-of-attack α. The reference parameters used for calculating the aerodynamic coefficients were the model plan-form area S_{ref}=0.3087m^2 and the model fuselage length from the leading edge of the nose cap to the base section L_{ref}=1.15m. The moment reference centre MRC of the model corresponded to 57% of the fuselage length. The maximum values of aerodynamic efficiency change from 4.5 to 4.0 with increasing Mach number from 3 to 8 whereas the stability in pitch decreases. The pitching moment coefficient C_m at Mach numbers 4 and 7 and different angles-of-attack are shown in Fig. 20 for a range of symmetrical aileron deflection angles δ = –18°…+6°. For the considered MRC position, the EFTV can be trimmed in pitch for angles-of-attack ranging from –6° to +6° by symmetrical flap deflection from +2.5° to –16° at Mach number M = 4, and from +4° to –12° at M = 7.

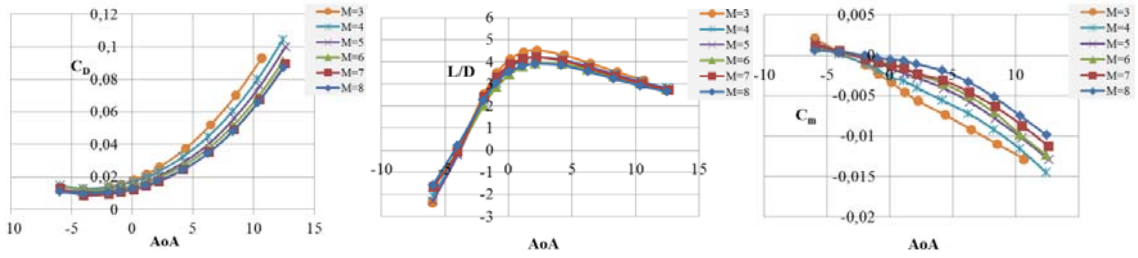


Fig. 19: Drag force coefficient C_D, aerodynamic efficiency L/D and pitching moment coefficient C_m of the glider vs. angle-of attack α. δ = 0^0.

Copyright © 2018 by the author(s)

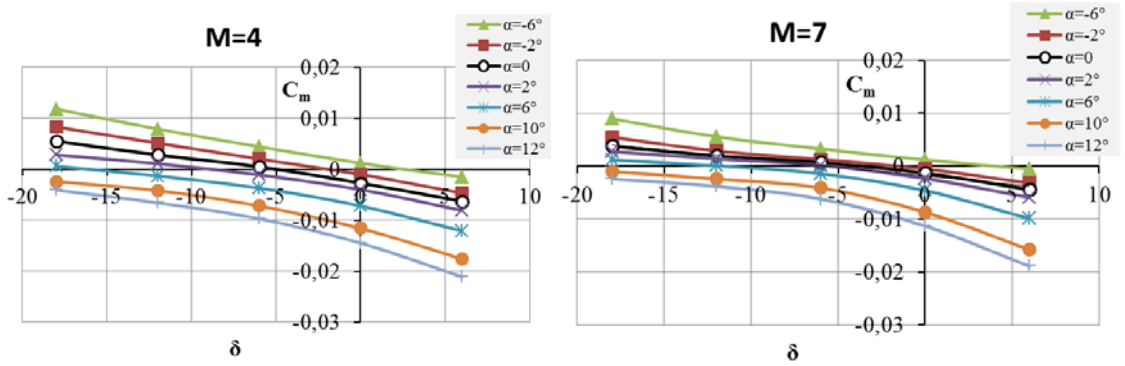


Fig. 20: Pitching moment coefficient of the glider model C_m vs. symmetrical flap deflection angle δ.

Additional experimental tests in T-116 were devoted to hypersonic boundary layer transition (BLT) with and without different transition grits installed near the nose/fuselage junction. A detailed description of the methodology and the results are presented in [13]. These tests were provided primarily at Mach number M=7. As an example, the photo of the forward part of the model with the transition grit consisting of cylindrical screws of 2mm diameter and the results of tests with different heights of screws k=0.35, 0.7 and 1.4mm are presented in Fig. 21. The points represent the experimental Stanton numbers obtained during tests in the symmetry plane on the windward side vs. local Reynolds numbers, whereas the lines correspond to calculated theoretical station values for laminar and turbulent boundary layers. Without any transition grit, the boundary layer is laminar for more than half of the model length, while transition grits promote BLT significantly earlier. The results were used to predict the position of BLT zone and heat transfer levels during the flight test.

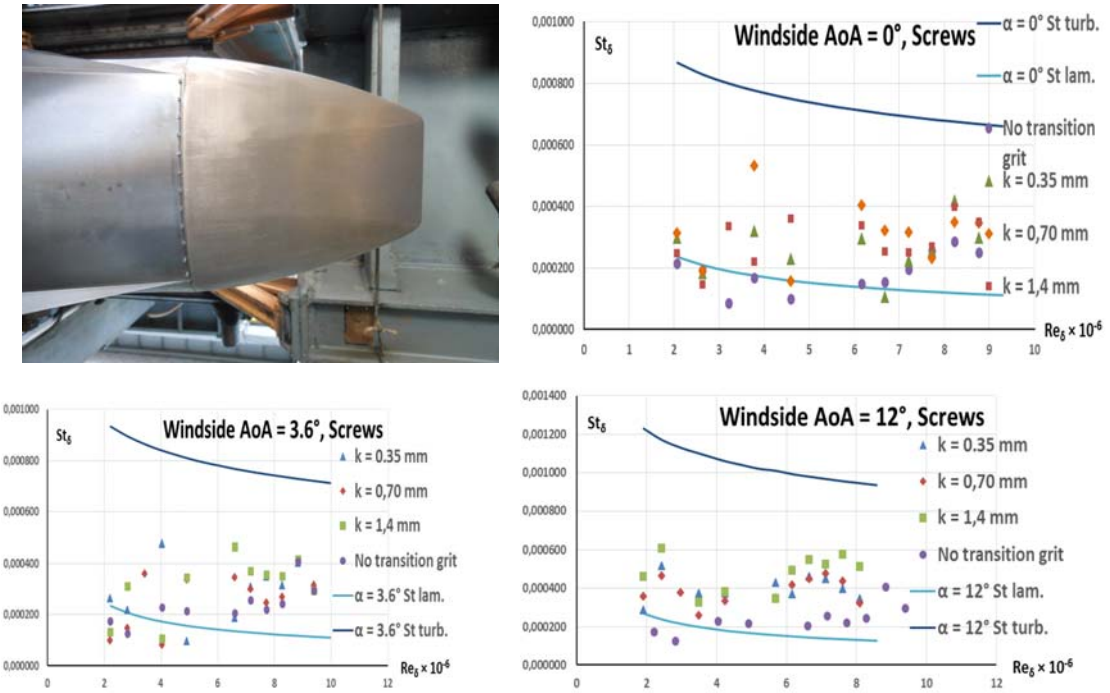


Fig. 21: Photo of the model with the transition grit installed (top left) and the results of tests: Stanton numbers vs. local Reynolds number; M = 7.

In parallel, the potential occurrence of transition triggered by irregularities or imperfections at the sharp leading edges was investigated in the HEG shockntunnel of DLR at Göttingen by means of temperature sensitive paint (TSP). Rather than protuberances creating perturbations in the boundary layer, most likely a large induced inviscid vortex was triggered at the root of the leading edge resulting into an increase heat transfer on the windward side (Fig. 22).

Copyright © 2018 by the author(s)

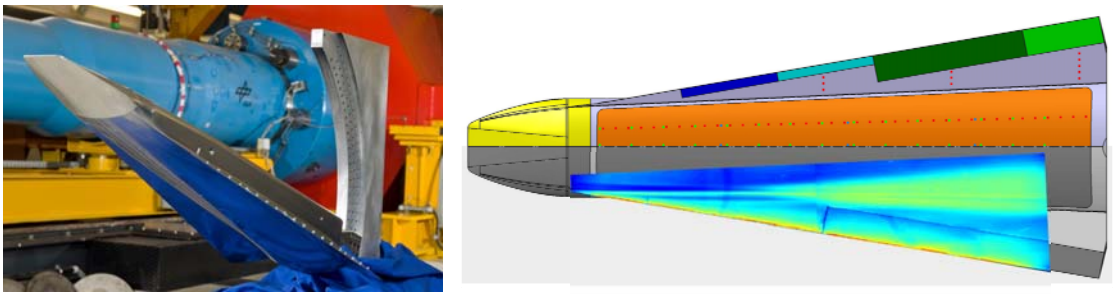


Fig. 22: Windtunnel model in front of HEG (top left) and the related wedged heat transfer increase.

2.6. EFTV/ESM Separation

To assure a clean separation between EFTV and ESM, the separation event was simulated for a flight Mach number of 6.9 at an altitude of 55km once the EFTV has the full aerodynamic control authority. The motion of both vehicle segments (EFTV and ESM) was simulated in an initial geodesic coordinate system. In former simulations only the motion of the ESM relative to the EFTV was taken into account. Starting from a steady-state initial solution with free-stream and flight state, an unsteady CFD/RBD simulation was initiated where both vehicles execute a 6DoF motion. The time step for the inviscid simulation is 5 ms and five coupling cycles were performed; the computational grid for the EFTV and ESM contains 61.4 and 20.5 million tetrahedrons, respectively. Different cases with an angle of sideslip AoS = 0° and 4° were investigated for the EFTV configuration with a flap deflection angle of FDA = 0° and/or −20°. To make sure that the angular rotation does not lead into a collision, the relative position of both parts were analysed. Fig. 23 shows the relative position and attitude of the ESM to the EFTV in steps of 0.25s after the initiation of the detachment for one of the studied cases. The different initial conditions lead to different pitch and yaw angles, nevertheless no contact either with the protruding vertical fins nor the flaps was detected. A roll motion of the EFTV is observed in the case of 4° sideslip. With -20° flap deflection a pitch-up of the EFTV is observed.

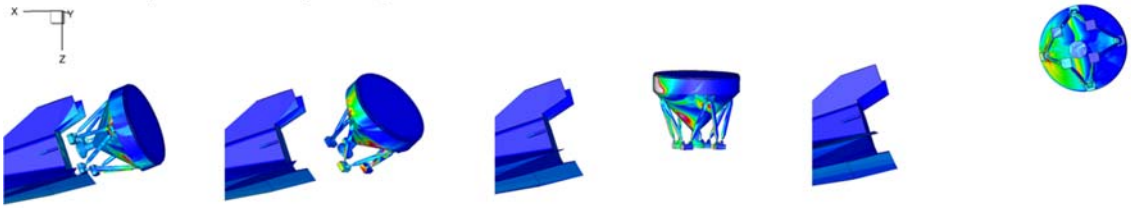


Fig. 23: EFTV/ESM separation for 0° flap deflection angle and 4° angle of sideslip in intervals of 0.25 s.

To verify and validate the above simulations, the separation process was also performed experimentally. Dynamically scaled models of the EFTV and ESM are manufactured at sub-scale, instrumented by UNSW with a miniaturized on-board inertial measurement unit (IMU), and flown in the short duration flow of a hypersonic wind tunnel TUSQ while being filmed by a high-speed schlieren optical visualization tool. The miniaturized IMU incorporates a tri-axial accelerometer and a tri-axial gyroscope as well as a dedicated microcontroller, power supply and blue-tooth module for communication. Internal ballast is used to tune the mass, CoG and moments of inertia of the model to ensure that the models are dynamically scaled [17] (see Fig. 24). A number of experimental campaigns were performed in the University of Southern Queensland's hypersonic wind tunnel (TUSQ) [18][19]. This compression-heated Ludwieg tunnel provides approximately 200ms of steady flow, with a start-up period of around 5ms. The model is released to fall under gravity toward the centreline of the Mach 6 nozzle, and then the tunnel is fired to produce the test flow in which the model then flies. The schlieren system provides both high-speed video for image tracking and simultaneous visualization of the flow structure around the model during the flight (see Fig. 24). Results from the image analysis of the free flight experiment and subscale CFD/RBD simulations are presented in Fig. 25 (left). Displacements in the X direction agree within the duration of the separation, as the ESM was detached at approximately 10 ms. As the displacement is calculated frame to frame, any slight measurement error will accumulate as the model is tracked for longer time durations. The right plot of Fig. 25 shows that the rotation occurs almost immediately. Rotation data from both image analysis and integrated gyroscope measurements show good agreement.

Copyright © 2018 by the author(s)

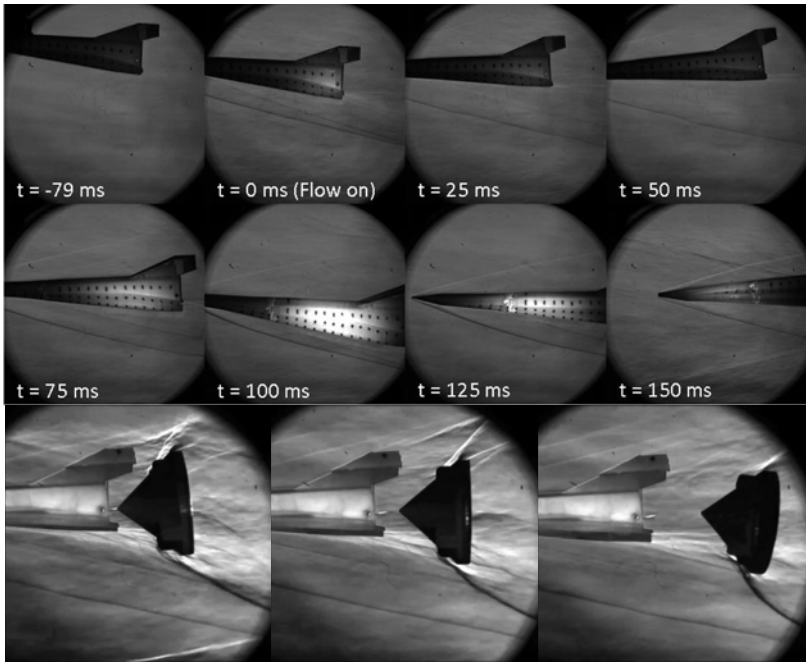


Fig. 24: Free flight of EFTV (top) and separation sequence of ESM from EFTV (bottom).

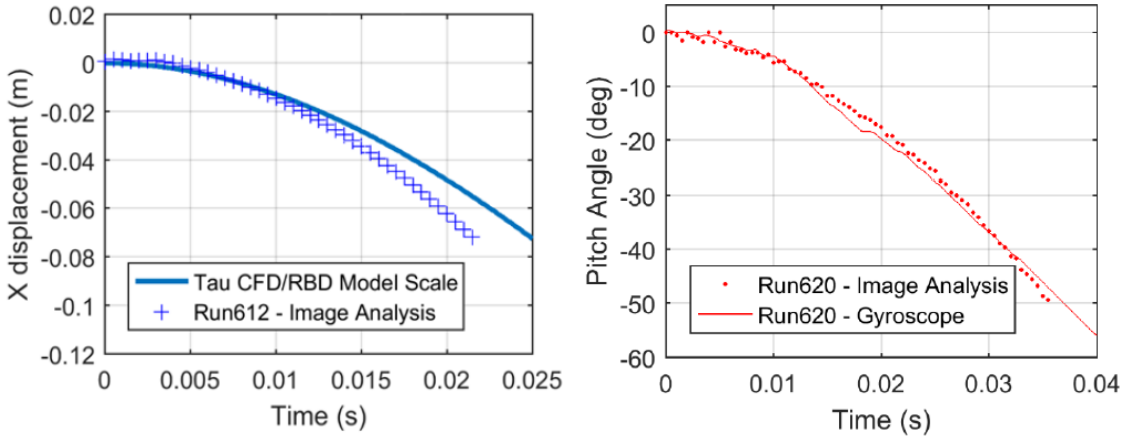


Fig. 25: ESM dynamics compared to results from CFD/RBD simulation (left) and ESM pitch movement comparison between on-board IMU and image analysis.

3. Low-Speed Flight Concept

3.1. Low-Speed Flight Experiments

As the project foreshadows a high-speed passenger vehicle [16], the EFTV needs to be stable throughout the entire flight envelope. Even though subsonic stability is often overlooked in hypersonic vehicles, it is crucial to obtain a viable final design. The low speed variant to be used for flight-testing was scaled to a length of 1.15m. Thus, the vehicle is large enough to be visible for the ground-based pilot. At the same time, it is small enough to be installed in the wind tunnel. As a propulsive system, an electric ducted fan with a diameter of 90mm is used. In combination with a battery consisting of ten Lithium Polymer cells connected serially, up to 42N uninstalled thrust is provided.

A full-scale wind tunnel model of the flying testbed was fabricated using an assembly of 3D printed pieces, which were then glued together and sanded for a smooth finish. Components such as the elevons and rudders are removable to allow the testing of various control settings. The rear portion of the ducting system was also removable to allow various pressure instrumentation to be installed. The

Copyright © 2018 by the author(s)

vehicle was mounted using an external adapter to the wind tunnel load cell. Fig. 26 shows the model mounted in the wind tunnel.

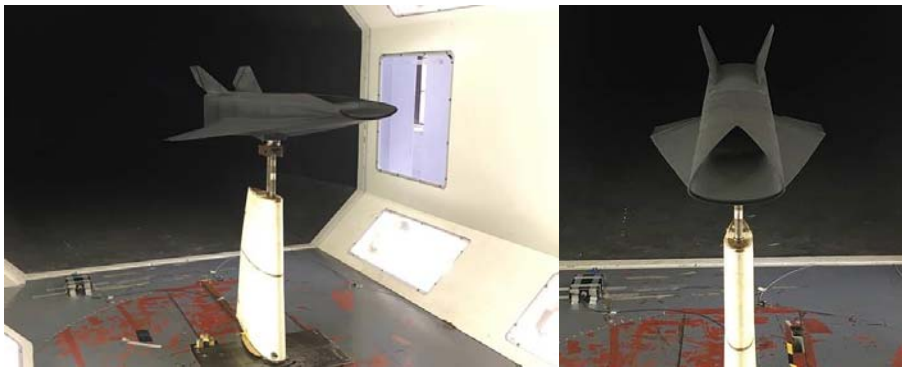


Fig. 26: Views of Vehicle in Wind Tunnel

The data acquired during testing was from load cell data to find aerodynamic and static stability coefficients, pressure data to characterise the internal flow path and tuft flow visualisation to determine the lip flow separation tendencies. Tests were conducted both with and without the fan installed to analyse its effects. During selected runs, total and static pressure measurements were taken to determine the nozzle jet velocity, flow quality at the fan face as well as the static pressure jump across the fan.

Fig. 27 shows the drag force variance with increasing airspeed based on the aircraft properties presented in Fig. 27. Cruise speed is selected to keep AoA below 5^0 while being speed stable. For this reason, a cruise speed of 21m/s is selected. The aircraft can be trimmed in this condition with -5^0 of elevon deflection. A take-off speed is determined to be ~16.5m/s at an AoA of 8^0. For landing, the AoA could be increased to lower the speed further than at take-off. Finally, the Oswald Efficiency Factor is 0.796, which is within the range of other delta-winged aircraft.

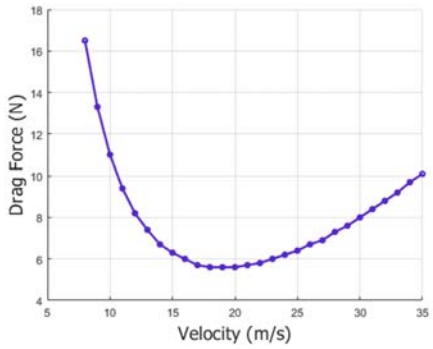


Fig. 27: Drag vs. velocity results for airframe only.

Fan tests were run to determine the installed thrust. Fig. 28 shows significant losses in thrust when increasing the AoA or the airspeed. The maximum thrust loss is ~46% for the lower power setting, as the fan begins to windmill and the flow separates from the intake lip. The higher power setting results in only ~ 27% thrust loss as the fan windmills less and extra suction delays the lip separation. Looking at Fig. 27 above, the thrust setting for a 10S Lipo system would be approximately 15A (between the two power settings shown below).

Both CFD and wind tunnel tests have confirmed the presence of a vortex originating at the top lip of the intake, which is ingested by the fan. This vortex is present at all tested airspeeds and AoA, but its location varies. Fig. 29 shows the CFD model for the vehicle at 0^0 AoA and a fan setting of 20A running on 8S lipo. The wind tunnel results compare well with CFD, showing the presence of these dual vortices. This may affect the fan performance when compared with an ideal inlet. The overall layout and implementation trade-offs are described at length in [25].

Copyright © 2018 by the author(s)

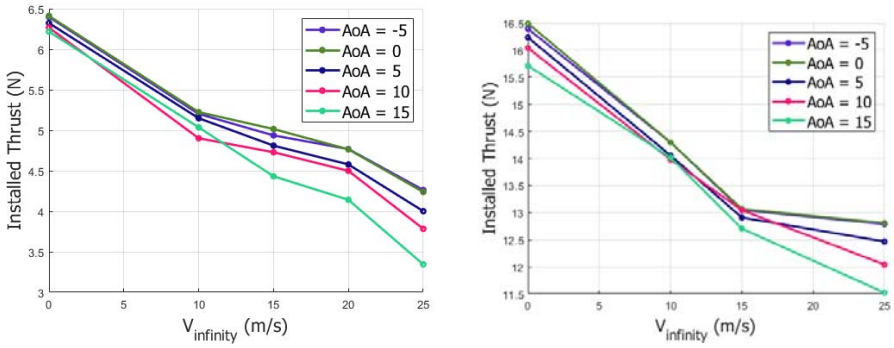


Fig. 28: Installed Thrust for 10SLipo with 10A (Left) and 20A (right)

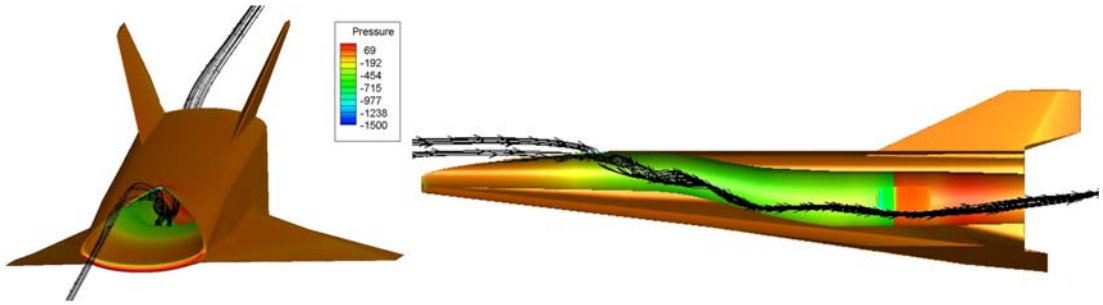


Fig. 29: Vortex originating from top inlet lip is ingested by the fan at 0^0 AoA and a fan setting of 20A

4. High-Speed Powered Concept

4.1. Aero-Propulsive Performance of the Powered Vehicle

TsAGI performed CFD studies of the 3m-long EFTV scramjet propelled configuration developed earlier within the European HEXAFLY Project [7]. Both laminar, transitional and turbulent simulations were performed. Numerical simulations have been conducted in the range of M_∞ =5÷8 and AoA = -2°÷8°. The Reynolds numbers calculated on the airframe body length correspond to the following values: $Re_L=6.88\cdot10^6$ ($M_\infty=5$), $Re_L=5.38\cdot10^6$ ($M_\infty=6$), $Re_L=7.66\cdot10^6$, $Re_L=7.33\cdot10^6$ ($M_\infty=7$) and $Re_L=5.92\cdot10^6$ ($M_\infty=8$). The computational grids of approximately 15 million elements are shown Fig. 30 where the intake area and the beginning of the internal propulsive path are also detailed.

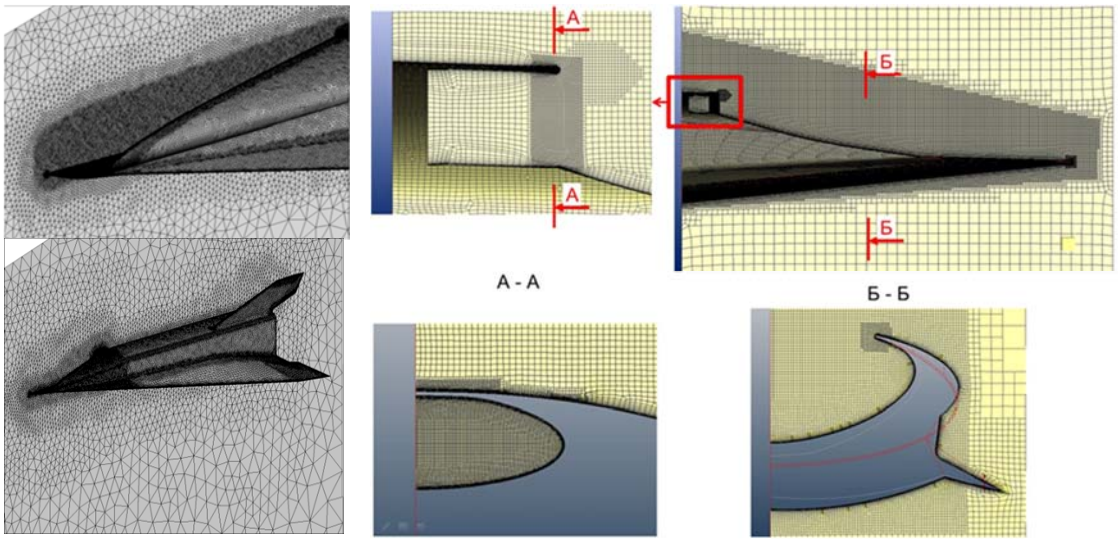


Fig. 30: Numerical grids for ANSYS-FLUENT (left) and NUMECA (right).

Copyright © 2018 by the author(s)

Flow field analyses show a peculiarity of a significant subsonic zone (represented by blue on pictures in Fig. 31), which occur in the air intake central part. The turbulent simulations have shown generally stable and regular flow in the air intake area.

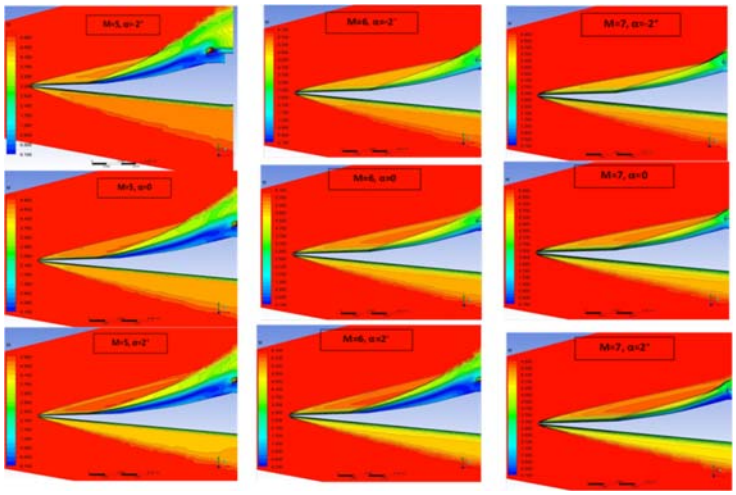


Fig. 31: FLUENT results: Mach number fields in the intake symmetry plane, M_∞=5, 6, 7; α=-2°, 0, 2°.

In addition, high intake mass flow rate coefficients (f) throughout the considered range of Mach number and AoA were predicted, see Fig. 27.

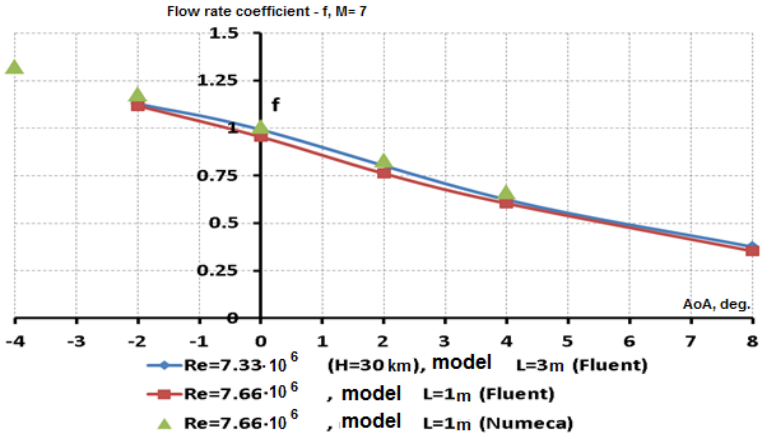


Fig. 32: Comparison of ANSYS-FLUENT and NUMECA results: the intake mass flow rate coefficient, f vs. angle-of attack, AoA. M_∞=7.

The general trend is that the mass flow rate decreases monotonically with increasing AoA. It is important to note that when AoA=0 and Mach number is M_∞= 7 or 8, the mass flow rate coefficient takes values close to 1, according to the results of both software packages ANSYS-FLUENT and NUMECA. At Mach M_∞= 6, a sharp decrease of the mass flow rate was predicted in the range of AoA=0÷2° showing that the intake unstarts at positive AoA.
Comparison of the Mach number contours at the intake entrance section obtained by the two codes is presented in Fig. 33. The results indicated a good agreement for basic parameters: intake mass flow rate coefficient, density, pressure and Mach number. As anticipated by the intake design requesting a turbulent boundary layer to cope with the compressive pressure gradient, laminar numerical simulations showed indeed the appearance of a separation zone which strongly effects the intake capture area at the combustor entrance and destroys its performance. This is clearly indicated in Fig. 34 showing the Mach number contours in the symmetry plane obtained by ANSYS-FLUENT with both laminar and turbulent BLs at M_∞=7 and AoA=0. In the case of laminar flow, a large subsonic region is visible, which extends downstream and blocks almost the whole intake entrance area. In the case of turbulent BL, only a small local subsonic zone appears near the intake surface.

Copyright © 2018 by the author(s)

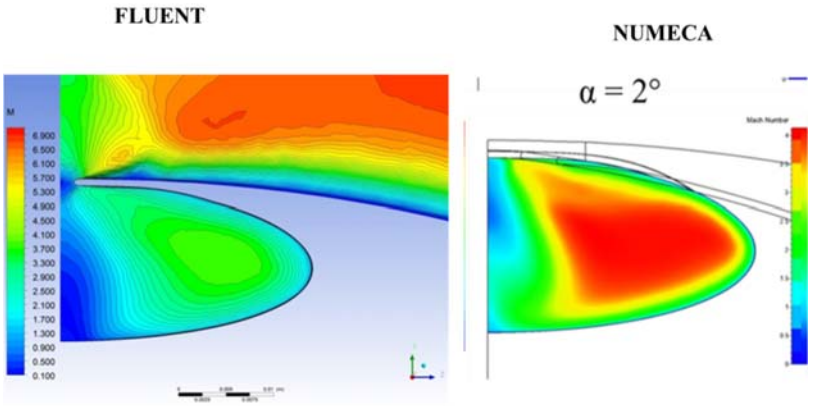


Fig. 33: Comparison of ANSYS-FLUENT and NUMECA results: Mach number contours at the intake entrance section, M_∞=7, α=2°.

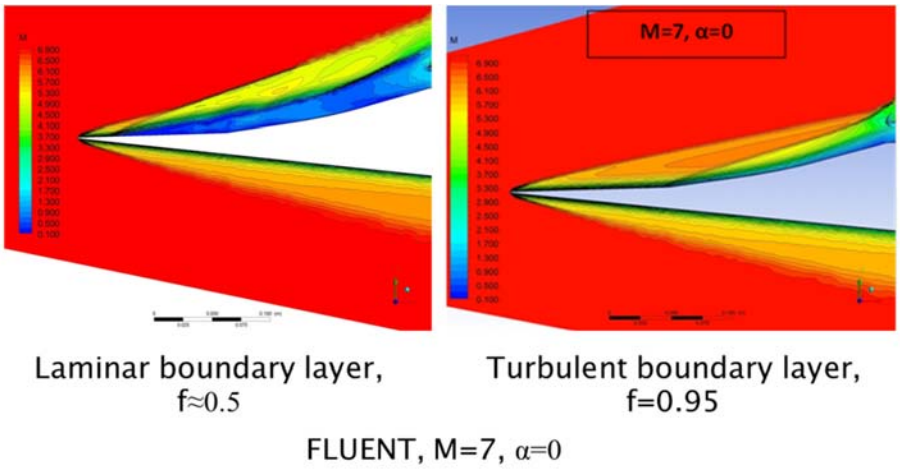


Fig. 34: Mach number contours: ANSYS-FLUENT results with laminar (left) and turbulent (right) BLs.

Comparisons of data on the intake mass flow rate coefficient extracted from numerical simulations (with preliminarily setting of turbulent and laminar BLs) and the experimental data obtained in the wind tunnel T-116 are shown in Fig. 35. Calculations with laminar BL gave significantly lower values of the intake mass flow rate coefficient f ≈ 0.5 ÷ 0.6. These results are much closer to the experimental data obtained on the model without BL tripping, which confirmed low mass flow rate coefficient and intake unstart at the most of test regimes due to the absence of a turbulent boundary layer on the intake.

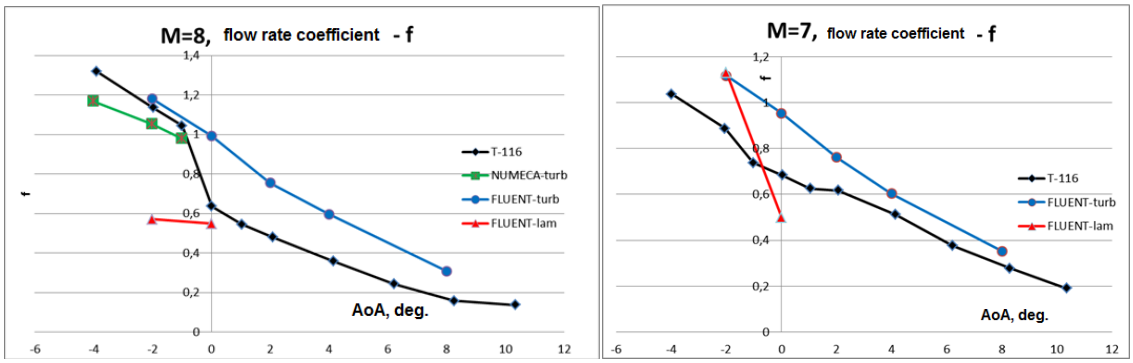


Fig. 35: Comparison of ANSYS-FLUENT results (turbulent and laminar BLs) with the experimental data: the intake mass flow rate coefficient, f vs. angle-of-attack, AoA. M_∞=8 and 7.

Copyright © 2018 by the author(s)

4.2. Aerodynamic Tests on the Powered Configuration

TsAGI performed also experimental investigation in their supersonic and hypersonic wind tunnel T-116 to assess the aerodynamic performance on a 0.35 scaled the EFTV scramjet propelled concept. The approximately 1m long model with the internal flowpath allowed investigating the intake characteristics and taking into account the influence of the air passage through the engine propulsive path on the external aerodynamics of the vehicle (see Fig. 36). The model was tested at Mach numbers 6, 7 and 8.

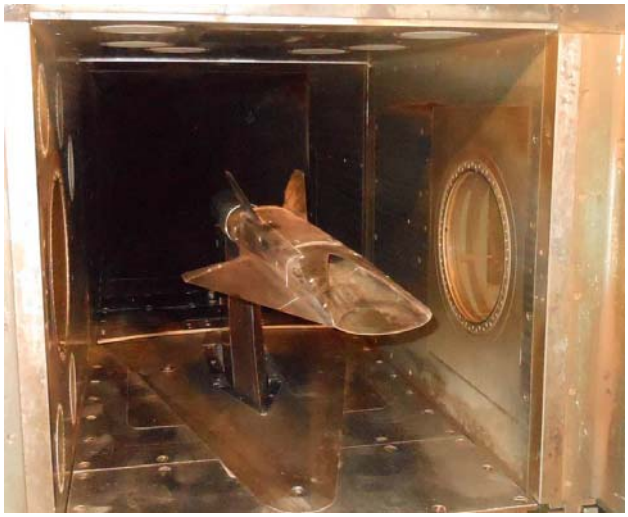
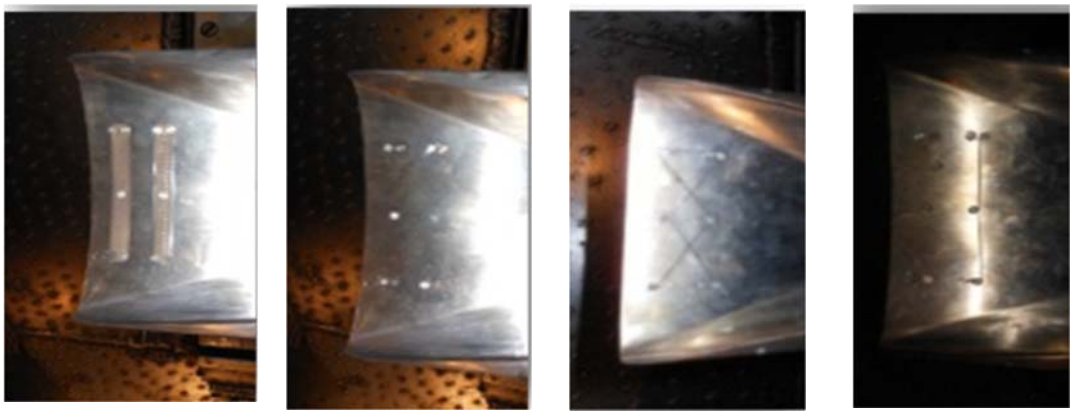


Fig. 36: Aerodynamic model of the EFTV scramjet propelled option installed in the test section of TsAGI T-116 Wind Tunnel.

The experimental results showed that the intake starting significantly depends on the BL state on the intake compression surface, i.e. laminar, transitional or turbulent. The first test series provided with 'clean' intake compression surface (without any BLT grit) showed that starting of the intake just appeared in a very limited range: at Mach 8 and negative AoA ≤ – 1°. At Mach number 7 and 6 the intake was unstarted.
A second test series was provided with different variants of transition grits, whose shapes are presented in Fig. 37. These included:

- 2 metallic strips with 3 rows of diamond-shaped roughness elements each; the heights of the roughness elements were 0.75mm and 1mm (var. 1),
- 10 screw heads of a 'dovetail' shape with height k=1.2mm and top diameter D = 3.8mm (var. 2),
- the same screw heads with wires of the diameter d = 0.5mm attached to the model surface by the screws in 'cross' position (var. 3) or
- in 'lines' position, i.e. parallel to the intake leading edge (var. 4).



Variant 1 Variant 2 Variant 3 Variant 4

Fig. 37: Different variants of the BLT grits used in the second test series.

Copyright © 2018 by the author(s)

The tests showed that transition grit variant 1 did not improve the intake starting performance, while all the other variants from 2 to 4 led to significantly wider ranges of test conditions at which the intake was started. The main test results obtained at Mach numbers 8 and 7 in terms of the intake mass flow rate coefficient *f* are shown in Fig. 38. Low values of f (less than approximately 0.6) indicate the absence of the intake starting. These results were obtained, however, with widened intake throat area corresponding to a contraction ratio CR = 7.4 being lower than that of the original intake (CR = 8.6).

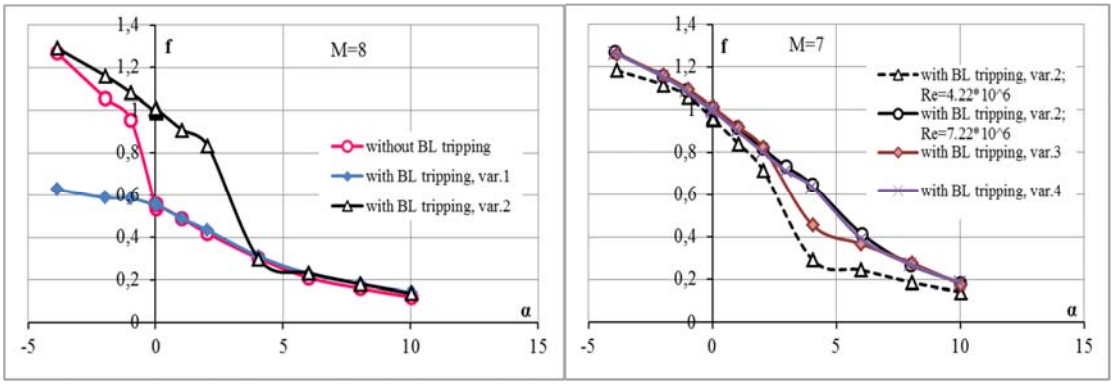


Fig. 38: The intake mass flow rate coefficient f vs. angle-of-attack α. Mach Numbers M_∞ = 8 and 7.

The external aerodynamics of the EFTV powered concept model was thoroughly investigated at Mach number 7. Its aerodynamic coefficients such as the drag force coefficient C_D, lift force coefficient C_L, aerodynamic efficiency L/D, and pitching moment coefficient C_m vs. angle-of-attack of the model α at zero sideslip and different symmetrical flap deflections are presented in Fig. 39. The reference parameters used for calculating the aerodynamic coefficients were the model plan-form area S_{ref}=0.2989m^2 and the model fuselage length measured from the leading edge of the intake to the base section L_{ref}=1.0066m. The moment reference centre MRC of the EFTV powered option model, similarly to that of the glider model, was located at 57% of the fuselage length.

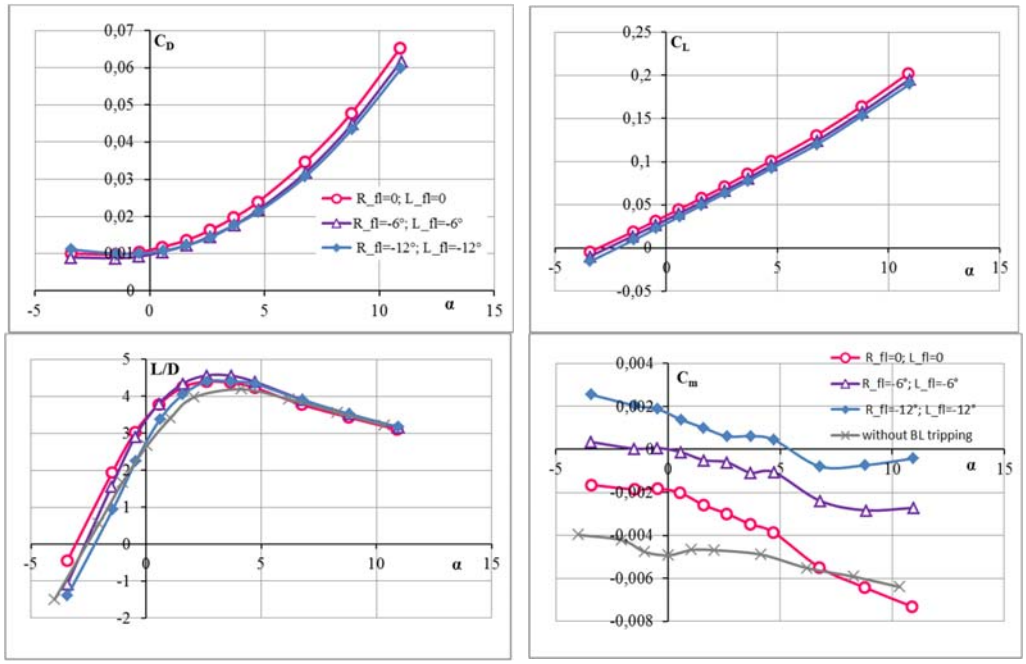


Fig. 39: Drag and lift force coefficients, C_D and C_L, aerodynamic efficiency, L/D and pitching moment coefficient, C_m vs. angle-of attack, α. M = 7, transition grit variant 2 with different right (R_fl) and left (L_fl) flap deflection, and without transition grit, R_fl = L_fl = 0.

Copyright © 2018 by the author(s)

It is seen that the maximum value of aerodynamic efficiency $(L/D)_{max}$ of the EFTV powered concept model with the transition grit variant 2 at M = 7 is about 4.5, and the vehicle can easily be trimmed on pitch at angles-of-attack up to 5° with moderate flap deflections. The model without transition grit displays the value of $(L/D)_{max} \approx 4.1$, and its trimming on pitch becomes problematic within the considering range of flap deflection angles.

4.3. Combustion Chamber Testing at the Connected Pipe Facility T-131 TsAGI

TsAGI also performed tests of the combustion chamber of the hydrogen-fuelled scramjet engine in the connected-pipe facility T-131. The model for these experimental tests was manufactured by CIAM, see Fig. 40. The main purpose of these experimental studies is to define the limits of stable operation of the combustion chamber. Beside this, it is also important to study the regimes at which self-ignition and flame stabilization are assured. The model with an elliptical combustion chamber is a full-scale model representing the actual size of the EFTV model. Such an approach makes it possible to conduct experimental investigations of the working principle without any adaptations. When mounted on the connected-pipe facility T-131, the combustion chamber is composed of eight separate sections interconnected through flanges (see Fig. 40): an intermediate part of the direct air heater, a part with critical section of the aerodynamic nozzle, supersonic part of the aerodynamic nozzle, a pre-injector section with two semi-struts, a section of combustion chamber with full-strut, a section of the 2D-nozzle and a section of the 3D-nozzle.

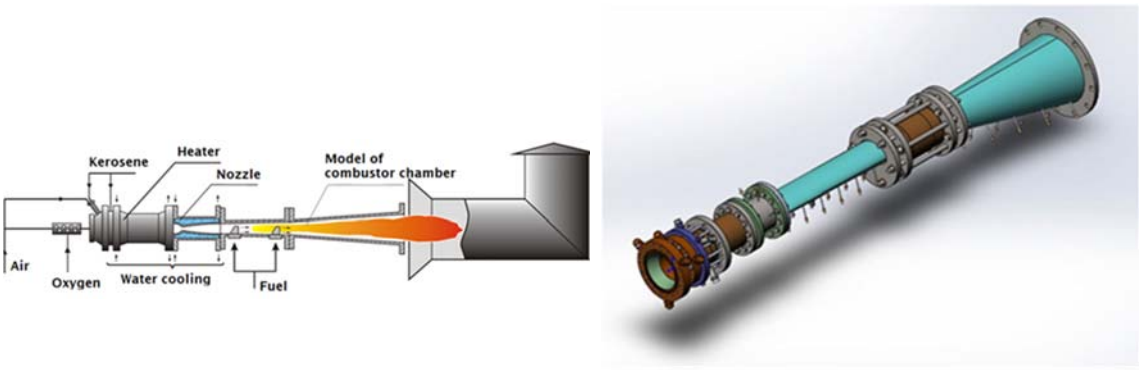


Fig. 40: Scheme of the T-131 facility (left) and model of the hydrogen combustion chamber for testing (right).

The T-131 facility (Fig. 40) is used mainly to study experimentally the operational process and the gas dynamics in ramjets and scramjets combustion chambers on the connected-pipe facility. The gas parameters in the air preheater of the test-bench allow simulating at the inlet of scramjet combustion chamber the total flow enthalpy, the M number and the pressure of flights in Mach number range 3÷10. Detailed description of the first test campaign can be found in [27].

During the first test series it was shown that the full-strut is located in the place with the maximum value of the static pressure in the model duct, which led to its burnout at parameters corresponding to the flight Mach number M = 7. Therefore, a new section was designed and manufactured in which the main fuel supply pylon was moved upstream as far as possible, based on the design limitations of the model (Fig. 37).

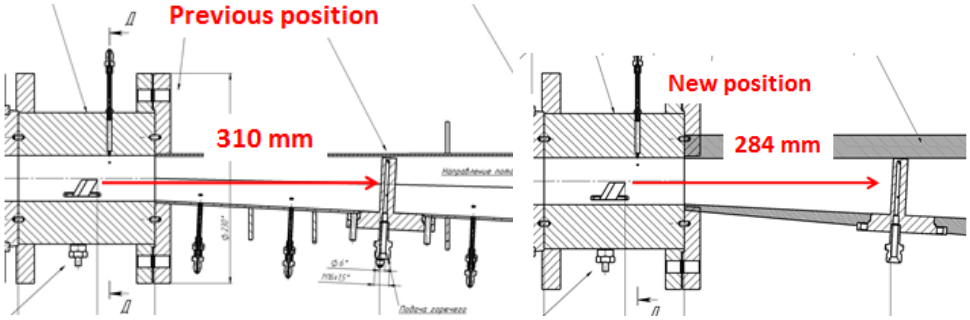


Fig. 37. New full-strut position

Copyright © 2018 by the author(s)

At the beginning of the test series, the runs were carried out with freestream conditions at the entrance of the model corresponding to the flight Mach number M = 6 with a fuel strategy similar to that in the previous series of tests (Figure 38). In addition, tests were carried out with a larger amount of fuel (close to the maximum possible, without knocking the flow into the aerodynamic nozzle of the facility) fed into the model (ER = 0.85) through the full-strut (35%). It is shown that in the investigated regimes the maximum value of the static pressure occurs between the fuel supply rows, closer to the semi-struts. At these conditions, once more fuel is being supplied through the full-strut, the efficiency of the working process is increased. This indicates the need for fuel combustion in the expanding part of the model duct.

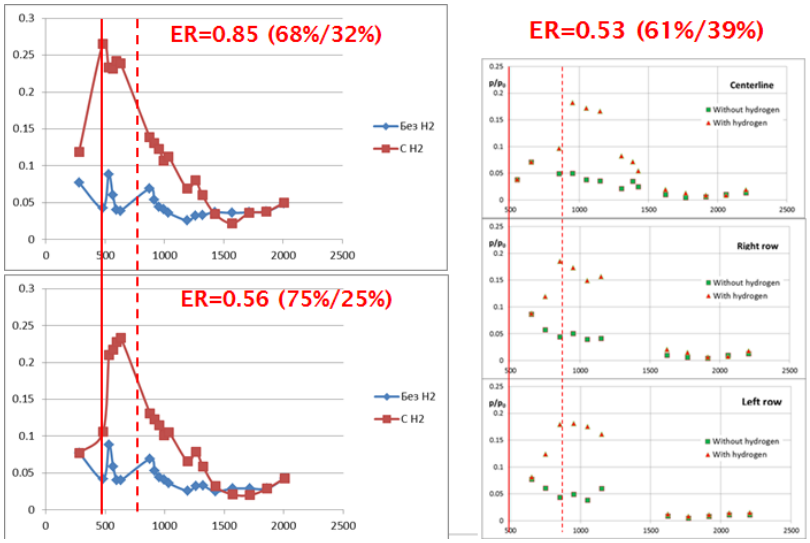


Fig. 38. Results at conditions correspond to the flight Mach number M=6

In several tests corresponding to a flight Mach = 7, the full-strut did not burn, which indicates a decrease in the thermal load on the strut and a displacement of the maximum value of the static pressure to the semi-struts. In the course of the tests, it was found that even at ER = 1.18, no knocking into the aerodynamic nozzle occurs, but even at ER = 0.74 the static pressure rise inside the model is insignificant (Fig. 39). It is shown that at ER = 1 it is necessary to supply more fuel through the full-strut, i.e. it is necessary to burn more fuel in a section with a constant cross section.

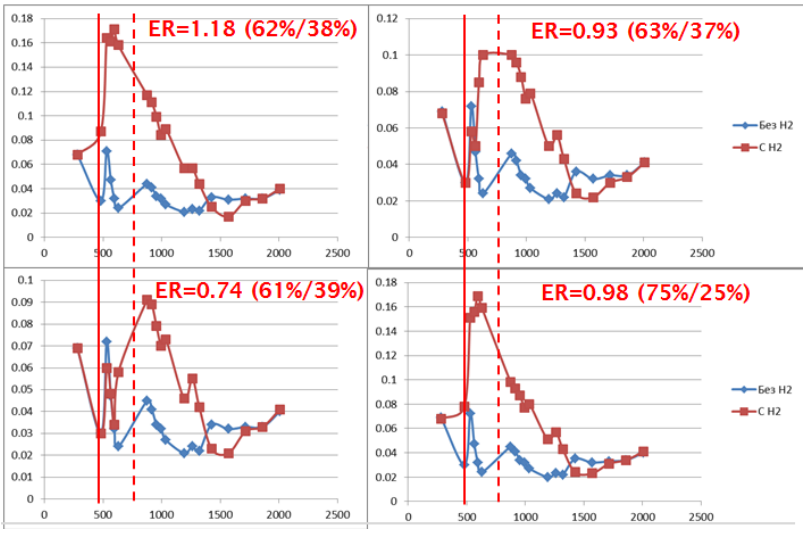


Fig. 39. Results at conditions correspond to the flight Mach number M=7

Copyright © 2018 by the author(s)

4.4. Propulsive Tests of the EFTV Powered Module in the CIAM Facility

Two different full-scale EFTV scramjet modules (Fig. 41 left) were designed and produced by CIAM for testing out in their free-jet ground test facility (Fig. 42). The purpose of these tests was the study of the operating conditions in the combustion chamber and the EFTV scramjet propelled option aero-propulsive balance demonstration [28]. The first model with simplified overall flowpath geometry [29] and having a low thermal inertia verified the principle operation of the scramjet module. It consisted of five main different parts: 1) air-intake with fuel pylon-injector; 2) combustion chamber; 3) nozzle; 4) frame; 5) power pylon. For the 2nd test, a scramjet model with a high-thermal heat sink capability was produced in CIAM (Fig. 41 right). The geometrical configuration of the combustion was made by an electro-erosive machine tool. The intake was milled out with help of a 5-coordinate turning machine. The manufactured parts were melted to each other. The intake, combustion chamber and nozzle are equipped with pressure sensors and thermocouples for gasdynamic structure and combustion research. Prior to the execution of the experimental campaign, a computational analysis was carried out to obtain the operating conditions for air-intake starting. A one-equation Spalart-Allmaras eddy viscosity model was used whereas the thermo-physical properties of the used gas are equal to fired heater combustion products properties. A sequence of numerical computations of EFTV scramjet module in the test bench [30] with conical nozzles were made. The nozzle accelerates the flow up to M=7.5. The air-intake was started during all investigated regimes (Fig. 43).



Fig. 41: The full-scale EFTV scramjet module with low (left) and high thermal heat inertia (right).



Fig. 42: Low thermal heat inertia scramjet module installation in the CIAM free-jet facility.

Copyright © 2018 by the author(s)

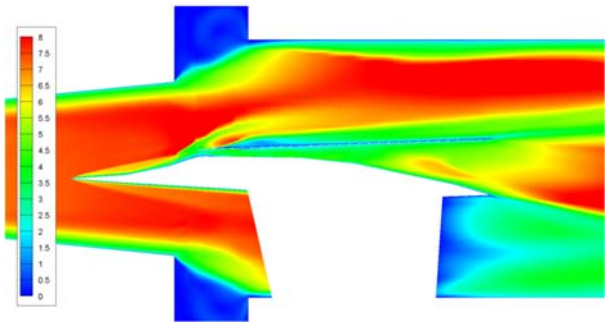


Fig. 43: Mach number contours in the symmetry plane for EFTV module flow in CIAM facility conditions.

The module was mounted on the thrust-measuring platform to determine the aero-propulsive balance. The main series of experiments was carried out with flow parameters corresponding to a flight altitude of the vehicle of H_∞=33 km. Particular attention was paid to dependencies of scramjet thrust from the equivalence ratio (ER) and mass flow rate schedule among the struts. A total of 18 runs were carried out, with the total pressure and the total temperature of the oncoming flow being respectively p* = 6.1 - 6.5 MPa and T* = 2310 K. The experiments were carried out with the installation of the facility module at an angle of attack α = -2°. Dependences of the resulting longitudinal force coefficient C_R on the angle of attack for different modes of engine operation are shown in Fig. 45.
The total force obtained in numerical simulation was compared with the experimental one, whose value with no fuel injection is -360 N. This 9% difference demonstrates an adequate accuracy of the calculation method.
During the tests, the equivalence ratio and the percentage of hydrogen flow through the fuel supply manifolds were varied. A total of 18 runs took place. During the runs the pressure in the vitiation heater was in the range P_{vh} = 6.1 to 6.5 MPa, the temperature T_{vh} = 2310 K. The modes and test results are shown in Table 2. The modes in which the positive aero-propulsive balance of the facility module was shown are bold. The positive aero-propulsive balance means that thrust generated by the engine, allowed exceeding the total aerodynamic drag of the facility model including support.

Table 2: Tests results

Point number	P_{vh}, [Mpa]	ER	Fuel injection through bands %	Stable working process	Force [N]
1	6.177	0.738	1/0	+	-161.8
2	6.283	1.208	0.65/0.35	+	-64.9
3	6.292	1.230	0.61/0.39	+	-43.4
4	6.310	1.291	0.66/0.34	+	-26.8
5	6.353	1.312	0.75/0.25	+	-7.3
6	6.362	1.432	0.77/0.23	-	-360.5
7	6.357	1.431	0.70/0.30	-	-355.7
8	**6.397**	**1.432**	**0.56/0.44**	**+**	**39.3**
9	**6.419**	**1.499**	**0.54/0.46**	**+**	**50.1**
10	**6.431**	**1.629**	**0.54/0.46**	**+**	**78.9**
11	6.428	1.141	0.40/0.60	-	-226.3
12	6.428	1.308	0.43/0.57	-	-136.9
13	**6.442**	**1.525**	**0.43/0.57**	**+**	**63.4**
14	**6.441**	**1.751**	**0.38/0.62**	**+**	**85.4**
15	6.461	1.183	0.91/0.09	-	-368.7
16	6.452	1.071	1/0	-	-367.4
17	6.474	1.028	0.68/0.32	+	-110.2
18	4.412	1.305	0.70/0.30	-	-109.9

P_{vh} – vitiation heater pressure,
ER – equivalence ratio,
Fuel injection through bands – percentage of fuel going through first/second fuel band,
Stable working process – means stable supersonic combustion in scramjet without thermal chocking,
Force – longitudinal force affected on facility module while fuel supplied

Copyright © 2018 by the author(s)

Positive aero-propulsive balance was demonstrated when the equivalence ratio ER was higher than 1.4. Effective thrust time history for ER=1.58 regime is shown in Fig. 44 (left). For combustion analysis, measured pressure distributions along the duct were obtained. On the right of Fig. 44, the pressure distributions with and without combustion are shown. High pressures in the duct in fuel supply case indicate clearly the presence of combustion, while the averaged flow is supersonic along the whole duct.

The blue lines on the graph Fig. 45 show the values of the numerically obtained external aerodynamic drag coefficients of the full vehicle (without taking into account the compression surface of the air intake device and the elements of the internal flow path). The black symbols show the values of the coefficient C_R, which were calculated at different coefficients ER = 0, 0.8, 1, 1.2. The red square and green triangle symbol are experimental points for ER = 1.0 and ER = 1.2 respectively. A positive aero-propulsive balance would lead to a negative C_R value. As can be seen from all the cases considered, this condition is satisfied by the values of C_R at the angle of attack α = -2 ° and ER = 0.8 and 1. However, once the same parameters are applied on the experimental values for the flowpath, it did not result in obtaining a positive aero-propulsion balance.

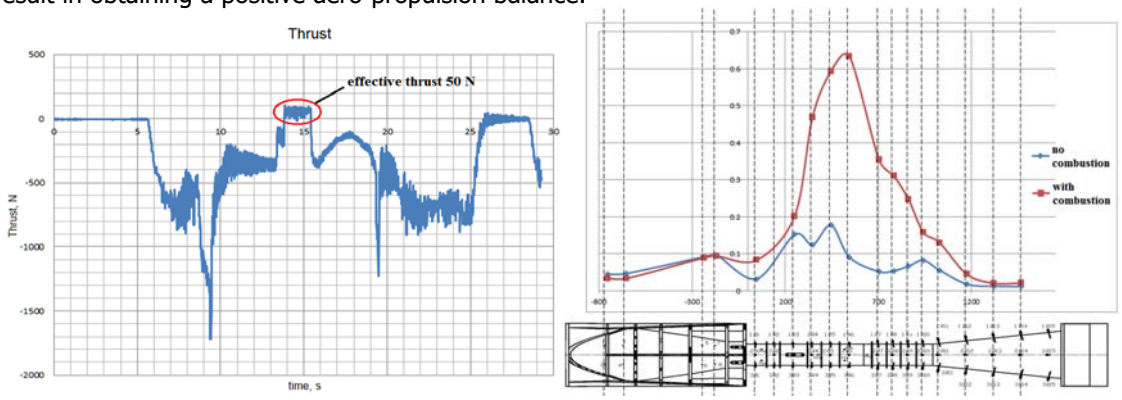


Fig. 44: Effective thrust to time dependence (left) and Pressure distribution along the duct (right)

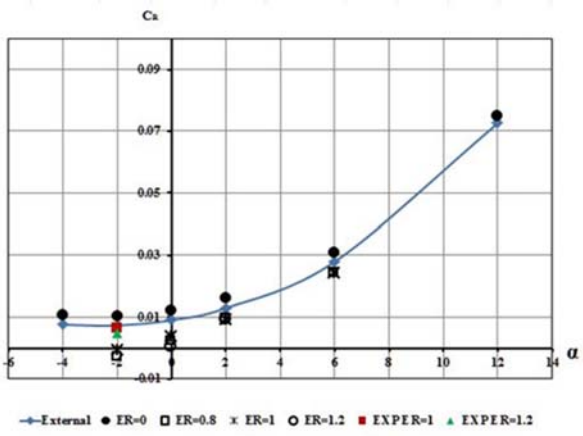


Fig. 45: Numerical and experimental data of the EFTV powered concept model at M = 7 with scramjet operation: resulting force coefficient C_R

In the experiments the values of the ER coefficient were varied which had a significant effect on the EFTV aero-propulsive balance. Fig. 46 shows the dependence of C_R on ER. As can be seen from the graph with increasing ER, the value of the C_R decreases due to the increase in thrust created by the engine. However, even at very high ER values, a positive aero-propulsive balance is not observed. The minimum value of the coefficient is C_R = 0.00267 at ER = 1.629 [31]. It should be noted that this value of C_R is relatively small and close to aero-propulsive balance [28]. It was shown earlier that the combustion efficiency in the experiments did not exceed η = 0.6 at the maximum ER. Even a slight increase of the combustion efficiency due to an improvement in the quality of the working process in

Copyright © 2018 by the author(s)

the combustion chamber will lead to a positive aero-propulsive balance of EFTV. Hence, it can be said that the proposed configuration is capable of providing a positive aero-propulsive balance. This will be the major objective with the high-thermal resource model during the 2nd test campaign.

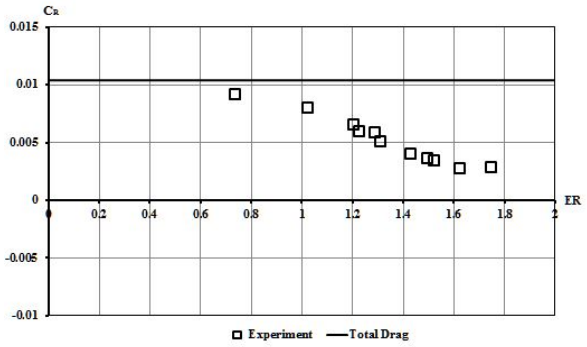


Fig. 46: Experimental resulting force coefficient C_R of the EFTV powered concept at M = 7with scramjet operation

4.5. Flight Control

A preliminary EFTV propelled flight trajectory was built by LII based upon estimates of aero-propulsive characteristics provided by TsAGI and CIAM, ensuring the achievement of scientific goals and satisfying the flight experiment constraints (Fig. 47).

The main purpose of this flight experiment is to study the engine subject to the constraints of 27 km <H <32 km, 7 <M <8 at a flight path angle γ close to zero. In the course of preliminary studies, it was shown that after the ESM separation the EFTV insertion into the engine research window is possible. However the model flight trajectory passes near the lower boundary of the research window both with respect to the M number and the flight altitude H. Maximization of the M number of the EFTV insertion into the engine research window resulted in the decrease of the insertion altitude and vice versa. Maximizing the altitude of the EFTV insertion into the engine research window resulted in a decrease of the insertion M number. Therefore, to cope with the problem of the trajectory selection, also the segment of the pull-out manoeuvre was considered in the optimization formulation in order to maximize the altitude of the EFTV insertion into the engine research window [27].

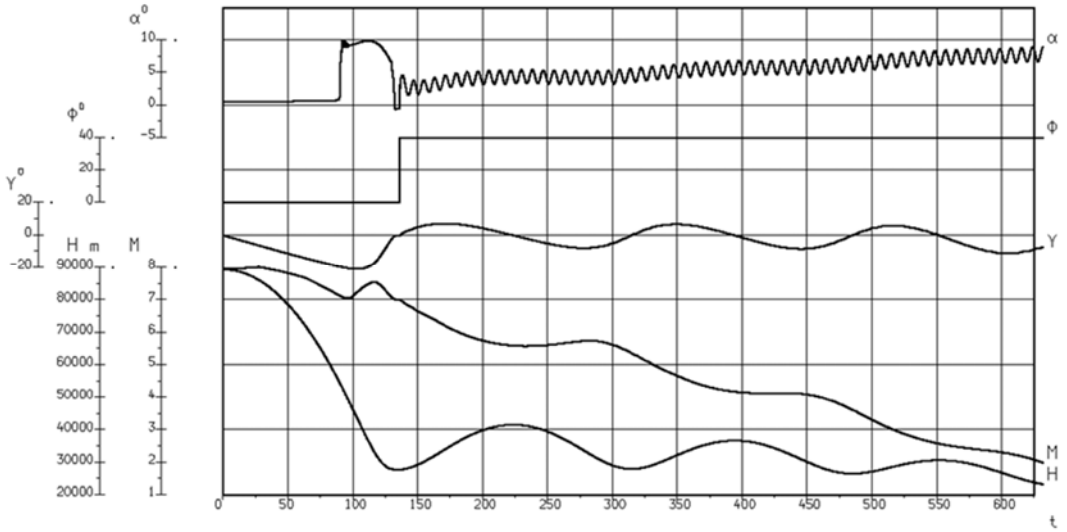


Fig. 47: Preliminary flight trajectory of the propelled EFTV

The optimized program α(t) applied in the EFTV longitudinal motion modelling, with due regard for the chosen algorithm of the automatic control system operation, allowed the EFTV to be inserted into the engine research window with parameters: M = 7.0, H = 27 900 m. In the engine research window at M=7 the EFTV flight takes place without loss of the M number and flight path angle; the selected

Copyright © 2018 by the author(s)

parameters of the autopilot provide the EFTV stabilization at the preset AoA =-0.5^0 after the engine start in less than 0.25 seconds.

After the engine is turned off, the further flight of the EFTV is carried out with a bank angle Φ of 40^0, which provides the necessary conditions for the telemetry data reception by ground TM stations throughout the entire flight of the EFTV. In this case, the idea is to apply a sinusoid perturbation on the angle of attack of the EFTV in the vicinity of the a priori estimate of the angle of attack α_{max}(M), corresponding to the maximum aerodynamic efficiency of the vehicle. It is expected that such an imposed perturbation will make it possible to refine the estimate of α_{max}(M) by the results of the flight experiment in the range of M numbers from 7 to 2.

5. Conclusions

The development status on a high-speed glider and a propelled concept at both low and high-speed were described.

The overall layout of the glider vehicle was generally discussed. The feasibility of a flight experiment for a glider concept in all its aspects was assessed based on numerical results and windtunnel campaigns. The use of a sounding rocket, a release at an apogee of 90km followed by a pull-out manoeuvre allows flight-testing the glider at Mach 7-8 at a flight altitude of about 30km.

The low-speed vehicle concept has shown both numerically and experimentally to have the necessary control authority. The selected electrical engine for the remote controlled vehicle can provide enough thrust during take-off and assure the feasibility of the low-speed flight tests in Australia.

The aero-propulsive performance of the propelled concept was also investigated numerically and experimentally. The outcome of the study indicated a positive thrust generation during the experiments at these high speeds but still needs to be proven for the fully equipped vehicle. The intake was shown to be sensitive to the transition location and needs to be triggered on the small scale to assure a representative flow field as originally designed.

Acknowledgements

This work was performed within the 'High Speed Experimental Fly Vehicles - International' (HEXAFLY-INT) project fostering International Cooperation on Civil High-Speed Air Transport Research. HEXAFLY-INT, coordinated by ESA-ESTEC, is supported by the EU within the 7th Framework Program Theme 7 Transport, Contract no.: ACP3-GA-2014-620327. The project is also supported by the Ministry of Industry and Trade, Russian Federation. Further information on HEXAFLY-INT can be found on http://www.esa.int/techresources/hexafly_int.

References

[1] Steelant J., "ATLLAS: Aero-Thermal Loaded Material Investigations for High-Speed Vehicles", *15th AIAA International Space Planes and Hypersonic Systems and Technologies Conference*, 28 April-1 May, 2008, Dayton, Ohio, USA, AIAA-2008-2582.

[2] Bouchez M., Dufour E., Le Naour B., Wilhelmi C., Bubenheim K., Kuhn M., Mainzer B., Riccius J., Davoine C. Justin J.-F., von Wolfersdorf J. Axtmann M., Villace F. and Steelant J., "Combustor Materials Research Studies for High Speed Aircraft in the European Program ATLLAS2", *20th International Space Planes and Hypersonic Systems and Technology Conference*, AIAA-2015-3639, 5-8 July 2015, Glasgow, UK.

[3] Steelant J., Dalenbring M. ., Kuhn M., Bouchez M. and von Wolfersdorf J., 'Achievements obtained within the ATLLAS-II Project on Aero-Thermal Loaded Material Investigations for High-Speed Vehicles', 21st Int. Space Planes and Hypersonic Systems and Technology Conference, AIAA-2017-2393, 6-9 March 2017, Xiamen, China.

[4] Steelant J., 'Achievements Obtained for Sustained Hypersonic Flight within the LAPCAT Project', 15th AIAA International Space Planes and Hypersonic Systems and Technologies Conference, AIAA-2008-2578, 28 April- 01 May 2008, Dayton, Ohio, USA.

Copyright © 2018 by the author(s)

[5] Steelant, J., Varvill, R., Defoort, S., Hannemann, K., and Marini, M., "Achievements Obtained for Sustained Hypersonic Flight within the LAPCAT-II project", *20th AIAA International Space Planes and Hypersonic Systems and Technologies Conference*, Glasgow, Scotland, July 6-9, 2015: AIAA-2015-3677.

[6] Pezzella, G., Marini, M., Cicala, M., Vitale, A., Langener, T., Steelant, J., "Aerodynamic Characterization of HEXAFLY Scramjet Propelled Hypersonic Vehicle", *32nd AIAA Aviation (Applied Aerodynamics Conference)*, 16-20 June 2014, Atlanta, GA: AIAA 2014-2844.

[7] Steelant, J., Langener, T., Di Matteo, F., Hannemann, K., Riehmer, J., Kuhn, M., Dittert, C., Scheuerpflug, F., Jung, W., Marini, M., Pezzella, G., Cicala, M., Serre, L., "Conceptual Design of the High-Speed Propelled Experimental Flight Test Vehicle HEXAFLY", *20th AIAA International Space Planes and Hypersonic Systems and Technologies Conference*, Glasgow, Scotland, 6-9 July 2015: AIAA-2015-3539.

[8] Roberto Scigliano , Giuseppe Pezzella, Sara Di Benedetto, Marco Marini, Johan Steelant, "HEXAFLY-INT Experimental Flight Test Vehicle (EFTV) Aero-Thermal Design", ASME International Mechanical Engineering Congress & Exposition (IMECE), IMECE2017-70392, 3-9 November 2017, Tampa, Floride, USA.

[9] Roberto Scigliano, Valerio Carandente, Design Analysis Of The Hexafly-Int Thermal Protection System, 8th European Workshop on TPS & Hot Structures, 19-22 April 2016, ESA/ESTEC, Noordwijk, The Netherlands.

[10] Favaloro, N., Rispoli, A., Vecchione, L., Pezzella, G., Carandente, V., Scigliano, R., Cicala, M., Morani, M., Steelant, J., "Design Analysis of the High-Speed Experimental Flight Test Vehicle HEXAFLY-International", *20th AIAA International Space Planes and Hypersonic Systems and Technologies Conference*, Glasgow, Scotland, 6-9 July 2015: AIAA-2015-3607.

[11] Pezzella, G., Marini, M., Reimann, B., Steelant, J., "Aerodynamic Design Analysis of the Hexafly-INT Hypersonic Glider", *20th AIAA International Space Planes and Hypersonic Systems and Technologies Conference,* Glasgow, Scotland, 6-9 July 2015: AIAA-2015-3644.

[12] Schettino A., Pezzella G., Marini M., Di Benedetto S., Villace V. F., Steelant J., Gubanov A. and Voevodenko N., 'Aerodynamic and Aerothermodynamic Database of the HEXAFLY-INT Hypersonic Glider', International Conference on High-Speed Vehicle Science and Technology (HiSST), 26-29/11/2018, Moscow, Russia, HiSTT-2018-2940957.

[13] Steelant J., Passaro A., Fernandez-Villace V., Gubanov A.A., Ivanyushkin D.S., Shvalev Yu.G., Voevodenko N.V., Marini M., Di Benedetto S. 'Boundary layer transition assessment on a slender high-speed vehicle', 21st Int. Space Planes and Hypersonic Systems and Technology Conference, AIAA-2017-2133, 6-9 March 2017, Xiamen, China.

[14] Pezzella, G., Carandente, V., Scigliano, R., Marini, M., Steelant, J., "Aerothermal Environment Methodology of the Hexafly-Int Experimental Flight Test Vehicle (EFTV)". *8th European Symposium on Aerothermodynamics for Space Vehicles*. 2-6 March 2015. Lisbon. Portugal. European Space Agency.

[15] Carandente, V., Scigliano, R., Pezzella, G., Marini, M., and Steelant, J., "Finite Element Thermal Design of the Hexafly-INT Experimental Flight Test Vehicle". *6th European Conference for Aeronautics and Space Sciences (Eucass)*. 29 June-3 July, 2015, Krakow, Poland.

[16] Steelant J. and Langener T., "The LAPCAT-MR2 Hypersonic Cruiser Concept", ICAS-2014-0428, *29th Congress of the International Council of the Aeronautical Sciences*, St. Petersburg, Russia, September 7-12, 2014.

[17] Kennell C., Neely A., O'Byrne S, Buttsworth D., 'Measurement of Vehicle Stability Coefficients in Hypersonic Wind Tunnels', *20th AIAA International Space Planes and Hypersonic Systems and Technologies Conference*, Glasgow, Scotland, 6-9 July 2015: AIAA-2015-3690.

[18] Kennell C., Neely A., Tahtali M., Buttsworth D.R., Choudhury R., "Free Flight Testing in Hypersonic Flows: HEXAFLY-INT EFTV", *AIAA SciTech*, AIAA 2016-1088.

[19] Buttsworth D.R., "Ludwieg Tunnel Facility with Free Piston Compression Heating for Supersonic and Hypersonic Testing", *9th Australian Space Science Conference 2009*, Published 2010.

[20] Nebula F., Morani G., Mattei G., Di Donato M.P., Rispoli A., Menchetti C. and Steelant J., 'Selection and Performance Evaluation of the Navigation unit for the HEXAFLY-INT Hypersonic Mission', 1st International Conference on High-Speed Vehicle Science and Technology (HiSST), 26-29/11/2018, Moscow, Russia.

[21] Di Benedetto S., Di Donato M. P., Rispoli A., Pezzella G., Scigliano R., Nebula F., Cristillo D., Cardone S., Steelant J., Villace V. and Vecchione L., 'Multidisciplinary Design and Flight Test of

Copyright © 2018 by the author(s)

the HEXAFLY-INT Experimental Flight Vehicle', 1st International Conference on High-Speed Vehicle Science and Technology (HiSST), 26-29/11/2018, Moscow, Russia.

[22] Andro J.-Y., Scigliano R., Kallenbach A. and Steelant J., 'Thermal Management of the Hexafly-Int Hypersonic Glider', 1st International Conference on High-Speed Vehicle Science and Technology (HiSST), 26-29/11/2018, Moscow, Russia.

[23] Andro J.-Y., Rotärmel W., Nebula F., Morani G., and Steelant J., 'Design of the Actuation System of the Hexafly-Int Hypersonic Glider', 1st International Conference on High-Speed Vehicle Science and Technology (HiSST), 26-29/11/2018, Moscow, Russia.

[24] Munk D. J., Vio G. A. , Verstraete D. and Steelant J., 'Structural Topology Optimisation of the HEXAFLY-INT Vertical Fin', 1st International Conference on High-Speed Vehicle Science and Technology (HiSST), 26-29/11/2018, Moscow, Russia.

[25] Bykerk T., Verstraete D., Wolf S., Villace V. and Steelant J., 'Performance and Stability Analysis of a Hypersonic Vehicle for a Low Speed Flight Test Program', 1st International Conference on High-Speed Vehicle Science and Technology (HiSST), 26-29/11/2018, Moscow, Russia.

[26] Choudhury R., Villace V. F. , Steelant J. and Buttsworth D., 'Micro-Aerothermodynamic Analysis of Protuberances on a Hypersonic Glider Using a Reduced Domain Approach', 1st International Conference on High-Speed Vehicle Science and Technology (HiSST), 26-29/11/2018, Moscow, Russia.

[27] M. A. Ivankin, A. A. Nikolaev, V. A. Talyzin and O. V. Voloschenko, 'Investigation of the Hydrogen Combustion Chamber Performance within the International HEXAFLY-INT Project', 30th Congress of the International Council of the Aeronautical Sciences (ICAS-2016), ICAS2016_458, Daejeon, Korea, 25th – 30th September, 2016

[28] Aleksandrov V.Yu., Kukshinov N.V., Prokhorov A.N., Rudinskiy A.V. Analysis of the integral characteristics of HEXAFLY-INT facility module. *21st AIAA International Space Planes and Hypersonic Systems and Technologies Conference*. Xiamen, China, March 6-9, 2017: AIAA-2017-2179.

[29] Aleksandrov V.Yu., Danilov M.K., Gouskov O.V., Gusev S.V., Kukshinov N.V., Prokhorov A.N., Zakharov V.S. Numerical and experimental investigation of different intake configurations of HEXAFLY-INT facility module. *30th Congress of the International Council of the Aeronautical Sciences (ICAS)*. Daegeon, Korea, September 26-30, 2016: ICAS-2016-0380.

[30] Aleksandrov V.Yu., Batura S.N., Gouskov O.V., Kukshinov N.V., Prokhorov A.N., Rudinskiy A.V. Complex numerical and experimental research of HEXAFLY-INT high-speed civil aircraft. *31th Congress of the International Council of the Aeronautical Sciences (ICAS)*. Belo Horizonte, Brazil, September 09-14, 2018: ICAS-2018-0672.

[31] Gubanov A.A., Ivanyushkin D.S., Kukshinov N.V., Prokhorov A.N., Talyzin V.A., Voevodenko N.V. Investigation on aero-propulsive balance for high-speed powered experimental flight test vehicle within the HEXAFLY-INT project. *31th Congress of the International Council of the Aeronautical Sciences (ICAS)*. Belo Horizonte, Brazil, September 09-14, 2018: ICAS-2018-0508.

Copyright © 2018 by the author(s)